

**WIND TURBINE WAKES:  
FROM NUMERICAL MODELING TO MACHINE LEARNING**

by  
Chi Yan

A dissertation submitted to the Faculty of the University of Delaware in partial fulfillment of the requirements for the degree of Doctor of Philosophy in Marine Studies

Summer 2018

© 2018 Chi Yan  
All Rights Reserved

**WIND TURBINE WAKES:  
FROM NUMERICAL MODELING TO MACHINE LEARNING**

by  
Chi Yan

Approved: \_\_\_\_\_  
Mark A. Moline, Ph.D.  
Director of the School of Marine Science and Policy

Approved: \_\_\_\_\_  
Estella Atekwana, Ph.D.  
Dean of the College of Earth, Ocean, and Environment

Approved: \_\_\_\_\_  
Douglas J. Doren, Ph.D.  
Interim Vice Provost for Graduate and Professional Education

I certify that I have read this dissertation and that in my opinion it meets the academic and professional standard required by the University as a dissertation for the degree of Doctor of Philosophy.

Signed: \_\_\_\_\_  
Cristina L. Archer, Ph.D.  
Professor in charge of dissertation

I certify that I have read this dissertation and that in my opinion it meets the academic and professional standard required by the University as a dissertation for the degree of Doctor of Philosophy.

Signed: \_\_\_\_\_  
I. Pablo Huq, Ph.D.  
Member of dissertation committee

I certify that I have read this dissertation and that in my opinion it meets the academic and professional standard required by the University as a dissertation for the degree of Doctor of Philosophy.

Signed: \_\_\_\_\_  
Tobias Kukulka, Ph.D.  
Member of dissertation committee

I certify that I have read this dissertation and that in my opinion it meets the academic and professional standard required by the University as a dissertation for the degree of Doctor of Philosophy.

Signed: \_\_\_\_\_  
Kyle Pressel, Ph.D.  
Member of dissertation committee

## ACKNOWLEDGEMENTS

First and foremost, I would like to thank my advisor, Dr. Cristina Archer, who offered me the opportunity to discover my better self, mentored me with patience, understanding, and respect, guided me not only in scientific research but also in life. You are not only an intelligent, professional, passionate expert in atmospheric science and wind energy, but also a trustworthy and warm friend. I could have never possibly completed my Ph.D. studies without you, it was an honor to work with you.

I would also like to thank Dr. Kyle Pressel, Dr. Tobias Kukulka and Dr. I. Pablo Huq for being my committee members and providing valuable insights and instructive advice during my Ph.D. studies. I am very grateful to all of you for taking time and effort to peer-review my work.

Many thanks go to my colleagues and friends, Niranjana Ghaisas, Ahmad Vassel, Shengbai Xie, Yang Pan, Dong Wang, Enhui Liao, Wenfang Lu, Lu Han, Lingsheng Meng, Nan Chen, Sicheng Wu and many others for your help and companion.

I want to express my deepest gratitude and appreciation to my parents. Mom and Dad, I would never be able to achieve this doctoral degree without your unconditional support. You have always been trusting me on each decision I made regardless of success or failure. It was your continuous encouragement that helped me climb one mountain after another. It was your love that kept me pushing my limit and found the road to success. I also want to thank my beloved wife, Yuening, who has been extraordinary brave and considerate in our long-distance relationship. Your determination and commitment have pulled me through low valleys, and made the tough journey full of sunshine. Thank you, my most beautiful fluffy Husky Mars, for bringing joy and happiness into my life.

Finally, I want to thank that young boy who loves science, for never stop dreaming, never stop learning, and never give up.

## TABLE OF CONTENTS

<b>LIST OF TABLES</b> . . . . .	<b>viii</b>
<b>LIST OF FIGURES</b> . . . . .	<b>ix</b>
<b>ABSTRACT</b> . . . . .	<b>xiii</b>
 <b>Chapter</b>	
<b>1 NUMERICAL MODELING OF COMPRESSIBILITY EFFECTS AROUND LARGE WIND TURBINES</b> . . . . .	<b>1</b>
1.1 Introduction . . . . .	1
1.2 Compressibility effects on blade aerodynamic properties . . . . .	8
1.2.1 The incompressible blade element moment (BEM) method . . . . .	8
1.2.2 The BEM method with the Prandtl-Glauert compressibility correction . . . . .	11
1.2.3 The three wind turbines . . . . .	11
1.2.4 Results . . . . .	12
1.2.5 Conclusions . . . . .	17
1.3 Compressibility effects on air density . . . . .	22
1.3.1 Numerical methods . . . . .	23
1.3.2 Single wind turbine cases . . . . .	25
1.3.3 Two aligned wind turbines . . . . .	34
1.3.4 Validation . . . . .	37
1.3.5 Conclusions and future work . . . . .	39
<b>2 A GENERAL METHOD TO ESTIMATE WIND FARM POWER USING NEURAL NETWORKS</b> . . . . .	<b>48</b>
2.1 Introduction . . . . .	48
2.2 Data and methods . . . . .	50
2.2.1 Pre-processing of the Lillgrund wind farm data . . . . .	50

2.2.2	Architecture and training of the neural network . . . . .	53
2.3	Results . . . . .	57
2.3.1	Traditional NN to estimate power at Lillgrund only . . . . .	60
2.3.2	GM-trained NN to estimate power at any wind farm . . . . .	62
2.3.3	Transfer learning: Application of the GM-trained NN to the Nørrekær wind farm . . . . .	63
2.4	Conclusions . . . . .	64
	<b>BIBLIOGRAPHY . . . . .</b>	<b>70</b>
	<b>Appendix</b>	
	<b>A SIMULATIONS OF ATMOSPHERIC BOUNDARY FLOW . . . . .</b>	<b>80</b>
	<b>B COPYRIGHT PERMISSION . . . . .</b>	<b>82</b>

## LIST OF TABLES

1.1	Aerodynamic properties of the NREL-5MW wind turbine based on incompressible blade element theory. . . . .	14
1.2	Aerodynamic properties of the Siemens SWT-2.3-93 wind turbine based on incompressible blade element theory. . . . .	15
1.3	Setup of the five cases considered, with different geostrophic and hub-height wind speeds ( $U_g$ and $U_{hub}$ ), rotational speed $\Omega$ , and tip speed ratio (TSR). The TSR value for Case 5 is for the front-row turbine only. . . . .	27

## LIST OF FIGURES

1.1	Workflow for a) incompressible, Boussinesq and b) compressible wind turbine modeling. Note that, in the Actuator Line Model calculation of blade-induced forces and in the turbine power calculation, density is a constant $\rho_0$ in a), but it is a three-dimensional, time-dependent, fully-resolved variable in b). . . . .	6
1.2	Velocities and forces on a blade element. The angle between the local relative velocity and the rotor plane is $\phi$ , the local twist angle of the blade element is $\gamma$ , and the angle of attack is given by $\alpha = \phi - \gamma$ . . . . .	10
1.3	Schematic of the blades of three wind turbines: Siemens SWT-2.3-93, Vestas V112-3.0, and NREL-5MW. . . . .	13
1.4	Algorithm for incompressible BEM (without the red block) and compressible corrected BEM (with the red block). . . . .	16
1.5	Effects of compressibility correction: a) power coefficient $C_p$ , b) thrust coefficient $C_t$ , c) power loss (%) and d) tip Mach number as a function of the tip speed ratio for the NREL-5MW wind turbine. . . . .	18
1.6	Effects of compressibility correction: a) power coefficient $C_p$ , b) thrust coefficient $C_t$ , c) power loss (%) and d) tip Mach number as a function of the tip speed ratio for the Siemens SWT-2.3-93 wind turbine. . . . .	19
1.7	Effects of compressibility correction: a) power coefficient $C_p$ , b) thrust coefficient $C_t$ , c) power loss (%) and d) tip Mach number as a function of the tip speed ratio for the Vestas V112-3.0 wind turbine. . . . .	20
1.8	Schematic of the computational domain (not to scale) for the single-turbine and two-turbine cases. Domain sizes are expressed as multiples of the diameter of the reference NREL 5-MW wind turbine ( $D=126$ m). The circles represent the turbine rotors. . . . .	26

1.9	Case 2: Horizontal cross-sections at hub height of: a) Comp wind speed, b) Incomp wind speed, and c) Comp - Incomp wind speed difference, all in $\text{m s}^{-1}$ . The $12 \text{ m s}^{-1}$ contour line is shown in black in a) and b). . . . .	28
1.10	Case 2: Vertical (a) and lateral (b) profiles of wind speed ( $\text{m s}^{-1}$ ) along the wake centerline at various distances downstream of the turbine (expressed as multiples of the turbine diameter $D$ ). The black dashed lines represent positions of the turbine hub and tips. . . . .	30
1.11	Case 2: a) vertical and b) lateral profiles of TKE ( $\text{m}^2 \text{ s}^{-2}$ ) along the wake centerline at various distances downstream of the turbine (expressed as multiples of the turbine diameter $D$ ). The black dashed lines represent positions of the turbine hub and tips. . . . .	31
1.12	Horizontal cross-sections of Comp - Incomp wind speed difference (left) and Comp - Incomp TKE difference (right) at hub height, normalized by $U_{hub}$ and $U_{hub}^2$ respectively, for the four single-turbine cases in Table 1.3. . . . .	33
1.13	Vertical cross-sections in the rotor plane of Comp - Incomp wind speed difference, normalized by $U_{hub}$ , for the four single-turbine cases in Table 1.3. . . . .	35
1.14	a) Power production of the four incompressible and four compressible single-turbine cases described in Table 1.3, normalized by the power of the incompressible cases. b) Effects of compressibility on the power coefficient $C_p$ from BEM (lines) and Comp/Incomp simulations (circles). . . . .	36
1.15	Case 5: horizontal cross-sections of: a) Comp - Incomp wind speed difference and b) Comp - Incomp TKE difference at hub height, normalized by $U_{hub}$ and $U_{hub}^2$ respectively, for the two-turbine case in Table 1.3. . . . .	44
1.16	Case 5: horizontal profiles of: a) wind speed ( $\text{m s}^{-1}$ ) and b) TKE ( $\text{m}^2 \text{ s}^{-2}$ ) at hub height for the two turbine case, starting at the position of the second turbine ( $4D$ after the first turbine). . . . .	45
1.17	a) Computational domain and location of the 48 turbines in the Lillgrund wind farm; and b) time-averaged horizontal velocity normalized by hub height wind speed with wind coming from $225^\circ$ using the compressible framework. . . . .	46

1.18	Time-averaged relative power simulated with the compressible framework versus observed for columns E-H at the Lillgrund wind farm. . . . .	47
2.1	Location and layout of the Lillgrund offshore wind farm located between Denmark and Sweden, with geometric properties (BR, BD) for northerly and easterly wind directions. . . . .	51
2.2	Architecture of the neural network, with two hidden layers (in green) containing 50 and 40 neurons. . . . .	54
2.3	Flowchart of the traditional deep neural network (NN) developed with the Lillgrund wind farm data. In the traditional NN, the inputs (wind speed and direction) and output (power) at the Lillgrund wind farm are used to train the NN, which ultimately can be used to estimate future power at Lillgrund with high accuracy. The traditional NN cannot be used at another wind farm. . . . .	58
2.4	Flowchart of the GM-trained NN developed with the Lillgrund wind farm data. In the GM-trained NN (include the red box), an additional step is needed to calculate BR and BD with the Geometric Model (GM), but then the trained NN can be used at any wind farm, not just at Lillgrund. . . . .	59
2.5	Relative power at Lillgrund from observations (blue dots) and predictions (colored lines) with: a) traditional NN and b) GM-trained NN. . . . .	61
2.6	Two-dimensional wind farm power curve predicted with the traditional NN for Lillgrund. . . . .	66
2.7	Relative power as a function of BR and BD: a) observed at Lillgrund at a wind speed of $8 \text{ m s}^{-1}$ ; b-f) predicted by the GM-trained NN at different wind speeds ( $8\text{-}12 \text{ m s}^{-1}$ ). . . . .	67
2.8	Location and layout of Nørrekær with geometric properties (BR, BD) at certain wind directions. . . . .	68
2.9	Relative power at the Nørrekær wind farm from observations (blue dots) and predictions (colored lines) with the GM-trained NN. . . . .	69

A.1	Computational domain for atmospheric boundary layer flow. Domain sizes are expressed as multiples of the diameter of the reference NREL 5-MW wind turbine (D=126 m). . . . .	80
A.2	(a) Horizontally-averaged wind speed of the incompressible and compressible frameworks, compared with the theoretical log-law. (b) Horizontally-averaged wind speed difference between the two frameworks (incompressible minus compressible). . . . .	81

## ABSTRACT

Two main topics are studied in this research. First, the importance of compressibility effects of large horizontal-axis wind turbines are systematically assessed using the Blade Element Moment (BEM) method and unsteady Reynolds-Averaged Navier-Stokes (RANS) simulations. Second, a deep neural network (NN) with transfer learning ability are proposed for efficient wind farm power estimation.

The tips of large horizontal-axis wind turbines can easily reach high speeds, thus raising the concern that compressibility effects may influence turbine wakes and ultimately power production. All past studies have assumed that these effects are negligible. In Chapter 1.2, compressibility effects are assessed in terms of blade aerodynamic properties and variable density separately. Using the BEM method, we find that under normal operating conditions (i.e., wind speed  $< \sim 15 \text{ m s}^{-1}$  and tip speed ratio TSR  $< \sim 12$ ) aerodynamic corrections to the lift and drag coefficients of the blades have a minimal impact, thus the incompressible coefficients are adequate. In Chapter 1.3, compressibility effects are assessed in terms of variable-density, numerical simulations of a single turbine and two aligned turbines, modeled via the actuator line model with the default aerodynamic coefficients, are conducted using both the traditional incompressible and a compressible framework. The flow field around the single turbine and its power performance are affected by compressibility and both show a strong dependency on TSR. Wind speed and turbulent kinetic energy (TKE) differences between compressible and incompressible results origin from the rotor tip region but then impact the entire wind turbine wake. Power production is lower by 8% under normal operating conditions (TSR $\sim 8$ ) and 20% lower for TSR $\sim 12$  due to compressibility effects. When a second turbine is added, the front turbine experiences similar effects as the single-turbine case, but TKE differences are enhanced while wind speed differences

are reduced after the second turbine in the overlapping wakes. These findings suggest that compressibility effects play a more important role than previously thought on power production and, due to the acceptable additional computational cost of the compressible simulations, should be taken into account in future wind farm studies.

In Chapter 2, a deep neural network is trained and validated using three years of one-minute observations of wind speed, direction, and power generated at the offshore Lillgrund wind farm (Sweden). In its traditional form, the NN is used to generate a new two-dimensional power curve, which predicts with high accuracy (error  $\sim 2\%$ ) the power of the entire Lillgrund wind farm based on wind speed and direction. By contrast, manufacturers only provide one-dimensional power curves (i.e., power as a function of wind speed) for a single turbine. The second innovative application is the use of a geometric model (GM) to calculate two simple geometric properties to replace wind direction in the NN. The resulting GM-trained NN has the powerful feature of being applicable to any wind farm, not just Lillgrund. A validation at the onshore Nørrekær wind farm in Denmark demonstrates the high accuracy (error  $\sim 6\%$ ) and transfer-learning ability of the GM-trained NN.

## Chapter 1

# NUMERICAL MODELING OF COMPRESSIBILITY EFFECTS AROUND LARGE WIND TURBINES

### 1.1 Introduction

Modern wind turbines are being built with longer blades, taller towers, and higher capacities than ever before, to deliver more energy in a more efficient way. Turbine manufacturers all over the world are building wind turbine blades that exceed 70 m in length, e.g., the MHI Vestas V164-8.0MW (rotor diameter  $D=164$  m) ([MHI Vestas Offshore Wind, 2016](#)), the Siemens SWT-8.0MW ( $D=154$  m) ([Siemens AG, 2016](#)), the special two-blade wind turbine Ming Yang SCD-6.0MW ( $D=140$  m) ([Offshore Wind, 2014](#)), and the prototype Adwen AD-8.0MW ( $D=180$  m) ([Adwen, 2016](#)). The tip speed of these powerful wind turbines can easily reach Mach numbers in the range of 0.2-0.3 under normal operating conditions (and even higher under high-wind conditions). At these Mach numbers, treating the flow near the wind turbine as incompressible is questionable, as compressibility effects are expected to arise and can affect the flow field as well as the performance of the wind turbines. The incompressibility assumption has been the gold standard in past studies of flow around turbines but it has never been evaluated before at such high tip speeds as we see today. This study is the first to systematically evaluate the limitations of incompressibility with respect to both aerodynamic coefficients of the blades and variable density.

The extraction of energy from the wind by a large wind turbine leaves a wake behind it, which propagates downstream and is characterized by lower wind speeds and higher turbulence than the ambient air. The behavior of the wind turbine wake and the possible interactions between different wakes in a large wind farm have been

extensively studied for more than three decades ([Vermeer et al., 2003](#)) via wind tunnel studies and computational simulations.

Experiments have been successfully conducted in wind tunnels to study wind turbine aerodynamics using scaled-down versions of small-size ([Ainslie et al., 1990](#); [Chamorro and Porté-Agel, 2010](#); [Chen and Liou, 2011](#)) and medium-size ([Haans et al., 2005](#); [Krogstad and Eriksen, 2013](#); [Cho and Kim, 2012](#)) rotors. Only two wind tunnel experiments were performed for full-size rotors, the National Renewable Energy Laboratory (NREL) Phase VI rotor ([Simms et al., 2001](#)) and the Model Experiments In Controlled Conditions (MEXICO) rotor ([Snel et al., 2007](#)). The main limitation of wind tunnel studies lies in the scale of the wind turbine models. Even the full-size rotors are much smaller than the turbine rotors used in the industry, which usually are  $O(100)$  m. When extending the wind tunnel measurements to real applications, scaling effects occur ([McTavish et al., 2013](#)).

Studying individual and clustered real-size wind turbines has been made possible by computational fluid dynamics (CFD). With CFD, representing large wind turbine rotors with high fidelity, i.e., fully resolving the geometry, rotation, and effects of the turbine blades, is possible in principle, but remains nearly impossible in practice because it is too computationally intensive, as reviewed in ([Sanderse et al., 2011](#)) and ([Vermeer et al., 2003](#)). For high Reynolds number flows, the length scale of the boundary layer that forms around the turbine blades is  $O(10^{-3})$  m, while the length scale of the atmospheric boundary layer (ABL) domain is  $O(10^3)$  m. The number of grid points required to properly simulate such a range of scales is enormous, although some parts of the domain can be resolved at coarser resolution. To overcome this computational impediment, parameterizations of the aerodynamic forces on the turbine have been therefore developed to reduce grid requirements. In general, the turbine rotor or blades can be represented by the Actuator Disk Model (ADM) or the Actuator Line Model (ALM). For both, the aerodynamic forces are obtained with the Blade Element Momentum (BEM) theory ([Glauert, 1935](#)). The original ADM uses a circular disk to simulate the rotor and the thrust force induced by the wind turbine is imposed to

the flow (Gómez-Elvira et al., 2005; Jimenez et al., 2008; Calaf et al., 2010); however, the rotational effects of the rotor are not taken into account. This limitation was overcome by another version of the ADM, in which both thrust and tangential forces are imposed to the flow (Sørensen and Kock, 1995; Masson et al., 2001; Alinot and Masson, 2002). The disadvantage of the ADM is that the aerodynamic forces imposed on the fluid are averaged over the rotor area whereas the actual location of the blades changes with time. With the ALM, drag and lift forces are calculated along actuator lines that represent the rotating blades, therefore the rotational effects and movements of the blades are taken into account (Sørensen and Shen, 2002; Troldborg et al., 2010; Lu and Porté-Agel, 2011). The ADM and ALM can be integrated with either the unsteady Reynolds Averaged Navier-Stokes (RANS) framework (Masson et al., 2001; Schluntz and Willden, 2015) or the Large Eddy Simulation (LES) framework (Calaf et al., 2010; Xie and Archer, 2015). Finite Element Method (FEM) (Hsu et al., 2014), Finite Difference Method (FDM) (Xie and Archer, 2015) and Finite Volume Method (FVM) (Churchfield et al., 2012a,b) have been used to solve the URANS and LES systems of equations, using the incompressible assumption.

Some efforts have been made to account for compressibility effects when modeling wind turbines and the flow around them, but either for small regions confined near the turbine blades or using certain simplifications or corrections. Wood (1997) assumed that compressibility effects, being due primarily to the rotation of the blades, would be confined to the region near the blades and performed calculations of aerodynamic properties at various wind speeds using BEM theory. He found that, when the wind speeds were of the order of  $30 \text{ m s}^{-1}$ , significant reductions in the wind turbine performance occurred due to compressibility. Leishman and Beddoes (1989) proposed a semi-empirical stall model in which compressibility effects were simply represented with a constant correction coefficient. Duque et al. (1999) performed successful simulations of compressible flow around a wind turbine blade (the NREL phase II rotor) but using the so-called “thin-layer” Navier-Stokes equations. Later Duque et al. (2003) simulated the flow around blade of the NREL phase VI rotor using both CAMRAD

II (a lifting-line code with a free wake model) and OVERFLOW-D (a compressible solver with low Mach-number preconditioning capability); the power prediction with OVERFLOW-D showed good agreement with measurements while CAMRAD II did not and modifications were needed. [Xu and Sankar \(2000\)](#) solved the viscous compressible flow equations over a small region around the rotor and the other part of the domain was modeled using an inviscid free-wake method. [Pape and Lecanu \(2004\)](#) performed 2D and 3D simulations of a two-bladed wind turbine with a compressible solver, developed by ONERA ([Cambier and Gazaix, 2002](#)), over a domain restricted to one 180° azimuthal sector by using periodic boundary conditions. Their 2D simulations showed good agreement with experiments whereas the 3D computations did not, especially in the high speed region. In summary, no information can be found in the literature about assessments of the compressibility effects around large wind turbines in a realistically-sized domain.

The most widely used, averaged or filtered, governing momentum equation for wind turbine and wind farm simulations is the incompressible, Boussinesq form of the Navier-Stokes equation as follows:

$$\frac{\partial}{\partial t} (\rho_0 \bar{u}_i) + \frac{\partial}{\partial x_j} (\rho_0 \bar{u}_j \bar{u}_i) = -\frac{\partial \bar{p}}{\partial x_i} + \frac{\partial}{\partial x_j} (\tau_{ij} + \tau_{t_{ij}}) + \bar{\rho} g_i + \rho_0 f_i, \quad (1.1)$$

where  $\bar{u}_i$  is the averaged or filtered velocity,  $\tau_{ij}$  is the mean or resolved laminar stress tensor,  $\tau_{t_{ij}}$  is the turbulent stress tensor,  $g_i$  is the gravitational acceleration,  $f_i$  is the body force from the turbine blade model (ADM/ALM), and, from the Boussinesq approximation, air density is assumed constant everywhere ( $\rho_0$ ) except in the gravity term ( $\bar{\rho}$ ). Next, the buoyancy term can be linked to temperature to give the final form of the three governing equations (continuity, momentum, and temperature equations):

$$\frac{\partial \bar{u}_i}{\partial x_i} = 0, \quad (1.2)$$

$$\frac{\partial \bar{u}_i}{\partial t} + \frac{\partial}{\partial x_j} (\bar{u}_j \bar{u}_i) = -\frac{1}{\rho_0} \frac{\partial \bar{p}}{\partial x_i} + \frac{1}{\rho_0} \frac{\partial}{\partial x_j} (\tau_{ij} + \tau_{t_{ij}}) + [1 - \beta (\bar{\theta} - \theta_0)] g_i + f_i, \quad (1.3)$$

$$\frac{\partial \bar{\theta}}{\partial t} + \frac{\partial}{\partial x_j} (\bar{u}_j \bar{\theta}) = -\frac{\partial q_j}{\partial x_j} - \frac{\partial q_{t_j}}{\partial x_j}, \quad (1.4)$$

where  $\bar{\theta}$  is the averaged or filtered potential temperature,  $\theta_0$  is the reference, constant, and uniform potential temperature,  $q_j$  is the mean or resolved heat flux,  $q_{t_j}$  is the turbulent heat flux,  $\beta$  is the coefficient of volume expansion.

Two problems arise when compressibility effects are taken into account. First, the body force  $f_i$  on the flow is equal and opposite to the force exerted by the ADM/ALM, which is calculated using tabulated airfoil lift and drag coefficients based on the incompressible assumption. Thus, these tabulated aerodynamic properties of each blade section can be safely used when the Mach number is small because the incompressible assumption is valid. However, the Mach number at blade sections near the tip of large wind turbines can easily reach up to  $\sim 0.2-0.3$ . Based on linearized, compressible, subsonic flow analysis, as the Mach number increases, both lift and drag coefficients of the airfoil will increase (Leishman, 2006), thus compressibility corrections need to be applied to these coefficients when modeling large wind turbines. This will be explained in more detail in Section 1.2.

Second, the body force  $f_i$  in the incompressible framework is a density-normalized force. However, to calculate torque, thrust, or power output of the turbine, the body force needs to be multiplied by air density, which in principle is different at each point and at each time. Because of the incompressible and Boussinesq assumptions, air density is treated as a constant and therefore the body force is simply multiplied by a constant reference density  $\rho_0$  (Fig. 1.1a). Choosing the value of this reference density is arbitrary and different reference air densities will cause a direct change in power prediction. For example, using  $1.23 \text{ Kg m}^{-3}$  instead of  $1.18 \text{ Kg m}^{-3}$ , a 4.2% change, will cause a direct increase in power of 4.2%, which is non-negligible in terms of power output. The compressibility effects due to variable density can only be accounted for by using a compressible framework where variable density is resolved in space and time and the turbine force is calculated directly as  $\bar{\rho} f_i$  instead of  $\rho_0 f_i$  (Fig. 1.1b), as will be

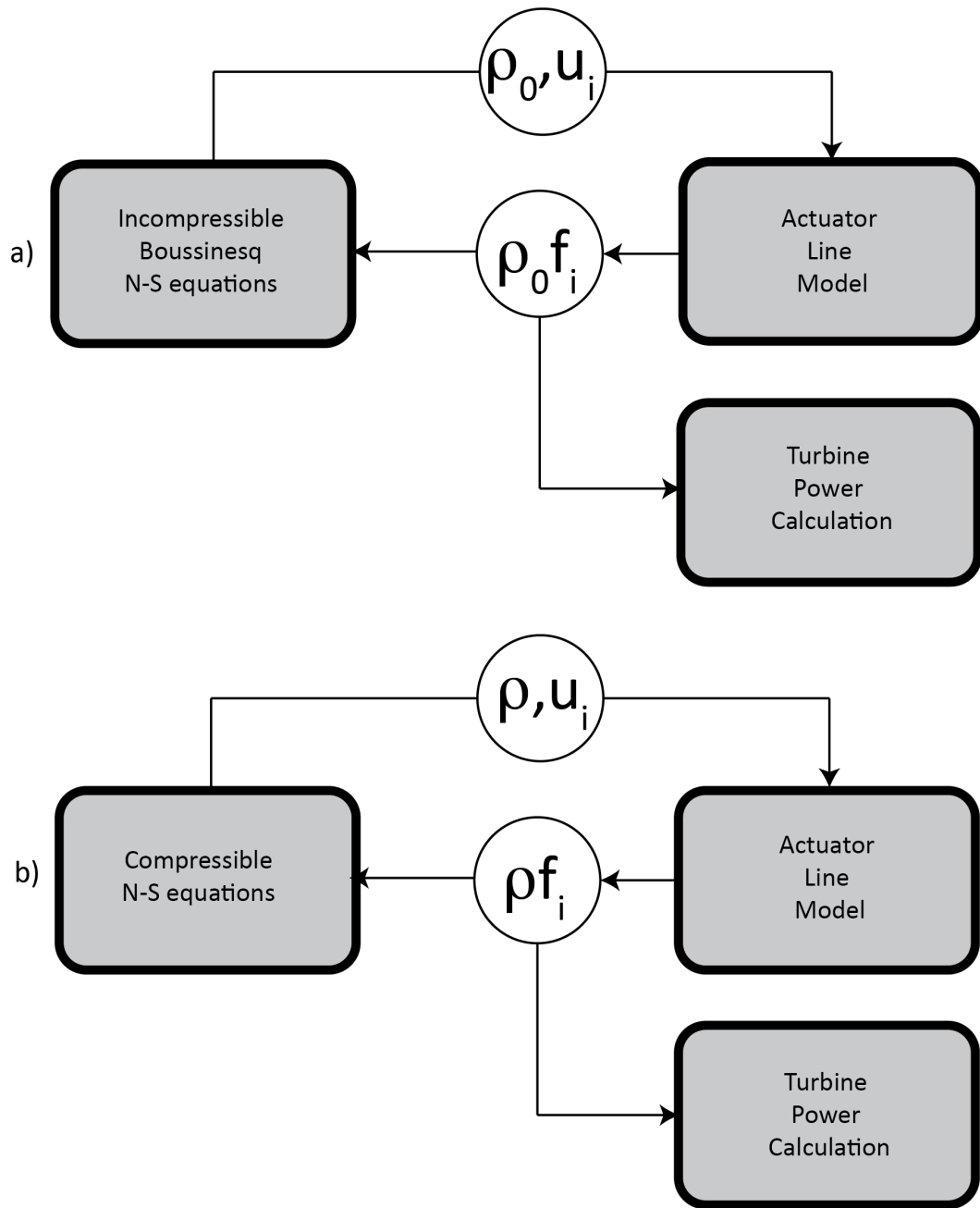


**Figure 1.1:** Workflow for a) incompressible, Boussinesq and b) compressible wind turbine modeling. Note that, in the Actuator Line Model calculation of blade-induced forces and in the turbine power calculation, density is a constant  $\rho_0$  in a), but it is a three-dimensional, time-dependent, fully-resolved variable in b).

done in Section [1.3](#).

## 1.2 Compressibility effects on blade aerodynamic properties

Today, bigger and bigger wind turbines are being built in order to deliver more energy in a more efficient way. At the same time, new challenges come along for numerical modeling of the bigger wind turbines. In general, wind turbines can be modeled using the Blade Element Moment (BEM) method, the Actuator Disk Model (ADM), and the Actuator Line Model (ALM). All these methods share one common assumption, i.e., air is incompressible. However, for a large modern wind turbine with blade length easily exceeding 50 m, the Mach number  $M$  (ratio of the fluid speed over the speed of sound) at the blade tips can be in the range of 0.2~0.4, where the incompressible assumption starts to fail and the compressibility effects may start to play a role. In this section, compressibility effects on blade aerodynamic properties are investigated.

### 1.2.1 The incompressible blade element moment (BEM) method

The BEM method is used to calculate the wind turbine performance with and without the compressibility correction. A blade element with radius  $r$  (Fig. 1.2) experiences a local relative velocity  $U_{rel}$ , which can be calculated as:

$$U_{rel}^2 = ((1 - a) U_0)^2 + ((1 + a') \Omega r)^2, \quad (1.5)$$

where  $\Omega$  is the rotational speed of the turbine,  $a$  is the axial induction factor, and  $a'$  is the rotational induction factor. Two corrections are necessary in order to obtain satisfactory values for  $a$  and  $a'$ . The first is Prandtl's tip loss factor,  $F$ , to account for the finite number of blades of a wind turbine, defined as  $F = a/a_b$ , where  $a$  is the average induction factor and  $a_b$  is the value at the blades. The second correction is called the Glauert correction, which is an empirical correction to the thrust coefficient for high axial induction factor values. Different forms of these corrections have been developed (Wilson and Lissaman, 1974; de Vries, 1979). Here we used the work of (Shen et al., 2005) and (Wang et al., 2009) to obtain the tip loss factor:

$$F = \frac{2}{\pi} \cos^{-1} \left[ \exp \left( \frac{N(r - R)}{2r \sin \phi} \right) \right], \quad (1.6)$$

where  $N$  is the number of blades. The induction factors are calculated as:

$$a = \frac{2 + Y_1 - \sqrt{4Y_1(1-F) + Y_1^2}}{2(1 + FY_1)}, \quad (1.7)$$

$$a' = \frac{1}{(1 - aF)Y_2 / (1 - a) - 1}, \quad (1.8)$$

where  $Y_1$  and  $Y_2$  are defined as:

$$Y_1 = 4F \sin^2 \phi / \sigma C_a, \quad (1.9)$$

$$Y_2 = 4F \sin \phi \cos \phi / \sigma C_{a'}, \quad (1.10)$$

with  $C_a = C_l \cos \phi + C_d \sin \phi$  and  $C_{a'} = C_l \sin \phi - C_d \cos \phi$ .

The power coefficient and thrust coefficient are calculated as:

$$C_p = \frac{\Omega Q}{\frac{1}{2} \rho A U_0^3}, \quad (1.11)$$

$$C_t = \frac{T}{\frac{1}{2} \rho A U_0^2}, \quad (1.12)$$

where  $Q$  and  $T$  are the total torque and thrust from the blade elements, given by:

$$dT = N (L \cos \phi + D \sin \phi) dr, \quad (1.13)$$

$$dQ = N (L \sin \phi - D \cos \phi) r dr, \quad (1.14)$$

where  $L$  and  $D$  are the lift and drag forces on the blade element  $dr$  (Fig. 1.2b). Note that an increase in both  $L$  and  $D$  would always cause an increase in the thrust but not necessarily an increase in the torque, due to the minus sign in Eq. 1.14. An iterative procedure is needed to solve these equations, as explained in [Manwell et al. \(2010\)](#).

The default, tabulated airfoil data used for incompressible calculations contain three important modifications that account for three-dimensional behaviors: the correction for rotational stall delay ([Du and Selig, 1998](#); [Eggers et al., 2003](#)), the extrapolation of the force coefficients using the Viterna's method ([Viterna and Janetzke, 1982](#)), and the incorporation of Beddoes-Leishman dynamic-stall model ([Jonkman et al., 2009](#)).

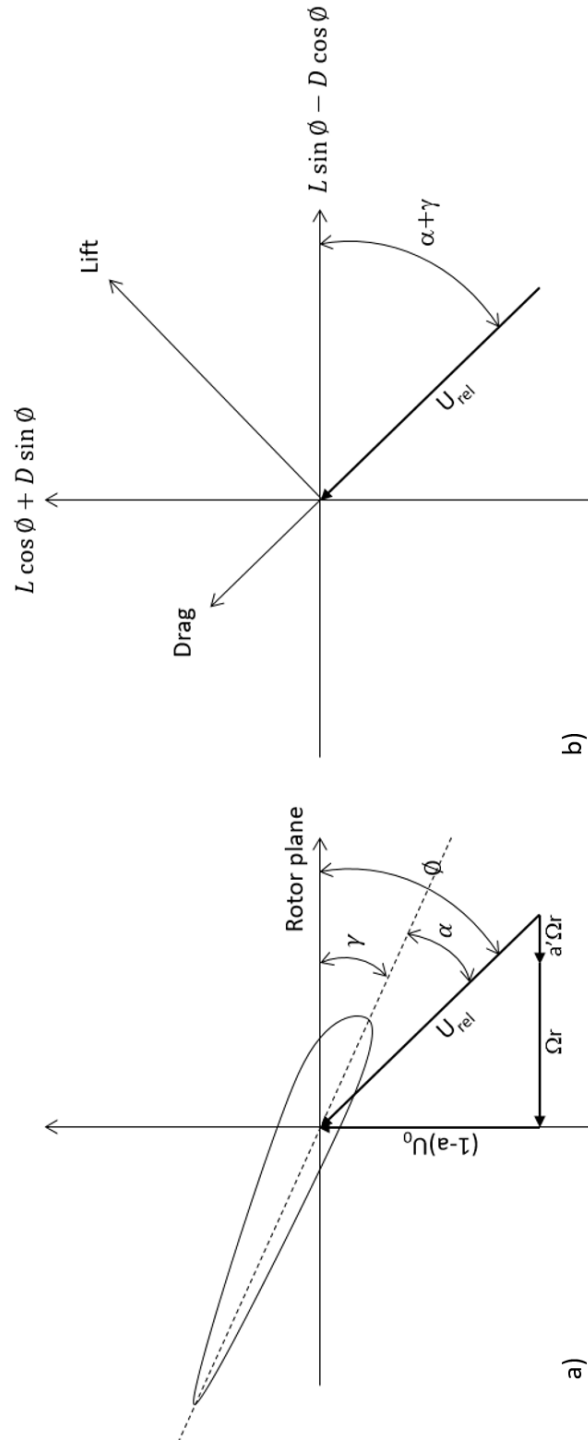


**Figure 1.2:** Velocities and forces on a blade element. The angle between the local relative velocity and the rotor plane is  $\phi$ , the local twist angle of the blade element is  $\gamma$ , and the angle of attack is given by  $\alpha = \phi - \gamma$ .

### 1.2.2 The BEM method with the Prandtl-Glauert compressibility correction

Although three types of corrections were already included in the tabulated aerodynamic properties described above, previous compressible subsonic flow research (Leishman, 2006) showed that, as the Mach number increases, both the lift and drag coefficients of an airfoil increase. This effect can be incorporated via the Prandtl-Glauert correction, in which both aerodynamic coefficients are functions of the local Mach number of the blade element  $M_B$  as follows:

$$C_l = \frac{C_{l,0}}{\sqrt{1 - M_B^2}}, \quad (1.15)$$

$$C_d = \frac{C_{d,0}}{\sqrt{1 - M_B^2}}, \quad (1.16)$$

where  $C_{l,0}$  and  $C_{d,0}$  are the lift and drag coefficients for incompressible flow. The local Mach number is:

$$M_B = \frac{U_{rel}}{c}, \quad (1.17)$$

where a constant speed of sound  $c=340 \text{ m s}^{-1}$  is generally used for atmospheric applications. More sophisticated corrections exist, such as the Karman-Tsien correction (Tsien, 1939; von Karman, 1941) and the Laitone correction (Laitone, 1951), but the Prandtl-Glauert is used here because of its simplicity and numerous applications.

### 1.2.3 The three wind turbines

Three wind turbines are studied here: the first one is the NREL-5MW research wind turbine, the second one is the Vestas V112-3.0 wind turbine, the third one is the Siemens SWT-2.3-93 wind turbine. A sketch of the blades of these three wind turbines is shown in Fig. 1.3. Since the turbine blade data are highly proprietary, for the Siemens SWT-2.3-93, Churchfield et al. (2012b) designed a 2.3-MW turbine to mimic the real Siemens turbine, which has a rotor diameter of  $D = 93 \text{ m}$ . The chord length distribution, pitch angle distribution, and airfoil types were well tested to get the turbine power curve very close to the real Siemens turbine. For the V112-3.0, Lu

and Porté-Agel (2011) also designed a 3.0-MW turbine with a diameter of  $D = 112$  m of similar characteristics to the real V112-3.0; however, for simplicity, this 3.0-MW turbine used a linear chord distribution (4 m to 0.5 m) and a linear twist distribution ( $17.5^\circ$  to  $0^\circ$ ). The NREL-5MW turbine blades were developed based on the DOWEC 6MW wind turbine blades (Kooijman et al., 2003; Lindenburg, 2002), with a diameter of  $D = 112$  m. Details of the blade section data are listed in Table 1.1 and Table 1.2.

#### 1.2.4 Results

Following the BEM algorithm in Fig. 1.4, the performances of the three wind turbines calculated with the Prandtl-Glauert compressibility corrections are compared with the performances using the standard incompressible assumption for uniform and constant flows with incoming wind speed  $U_0 = 5, 10, 15,$  and  $20 \text{ m s}^{-1}$  and for Tip Speed Ratio (TSR) ranging from 0.25 to 16 with a 0.25 interval.

The well-designed NREL-5MW wind turbine shows a very good efficiency when the incoming wind speed is low (e.g.,  $5 \text{ m s}^{-1}$ ); compressibility losses, manifested as a decrease in the power coefficient  $C_p$ , are barely noticeable even at the highest TSR of 16, as indicated by the almost perfect overlap of the blue and black-dashed lines in Fig. 1.5a. As the wind speed increases, the power losses remain negligible at low TSR ( $< 8$ ), but become more and more significant starting around a TSR of 8, as shown by the larger separation between the purple and the black-dashed lines in Fig. 1.5a. Using a threshold of 5% power losses (indicated by the green-dashed line in Fig. 1.5c), defined as the percent difference between compressible and incompressible power, we conclude that, for wind speed lower than approximately  $15 \text{ m s}^{-1}$  and TSR smaller than approximately 12, no correction is needed for the default incompressible tabulated data in terms of power production. On the other hand, at high wind speeds ( $> \sim 15 \text{ m s}^{-1}$ ) with a large TSR ( $> \sim 12$ ), compressibility effects are not negligible and power losses exceed 20% and can be as high as 50%. This is due to the increase in both lift and drag coefficients associated with the increased tip Mach number (Eq. 1.15 and Fig. 1.5d), which causes: an increase in the thrust coefficient (Fig. 1.5b) and in the

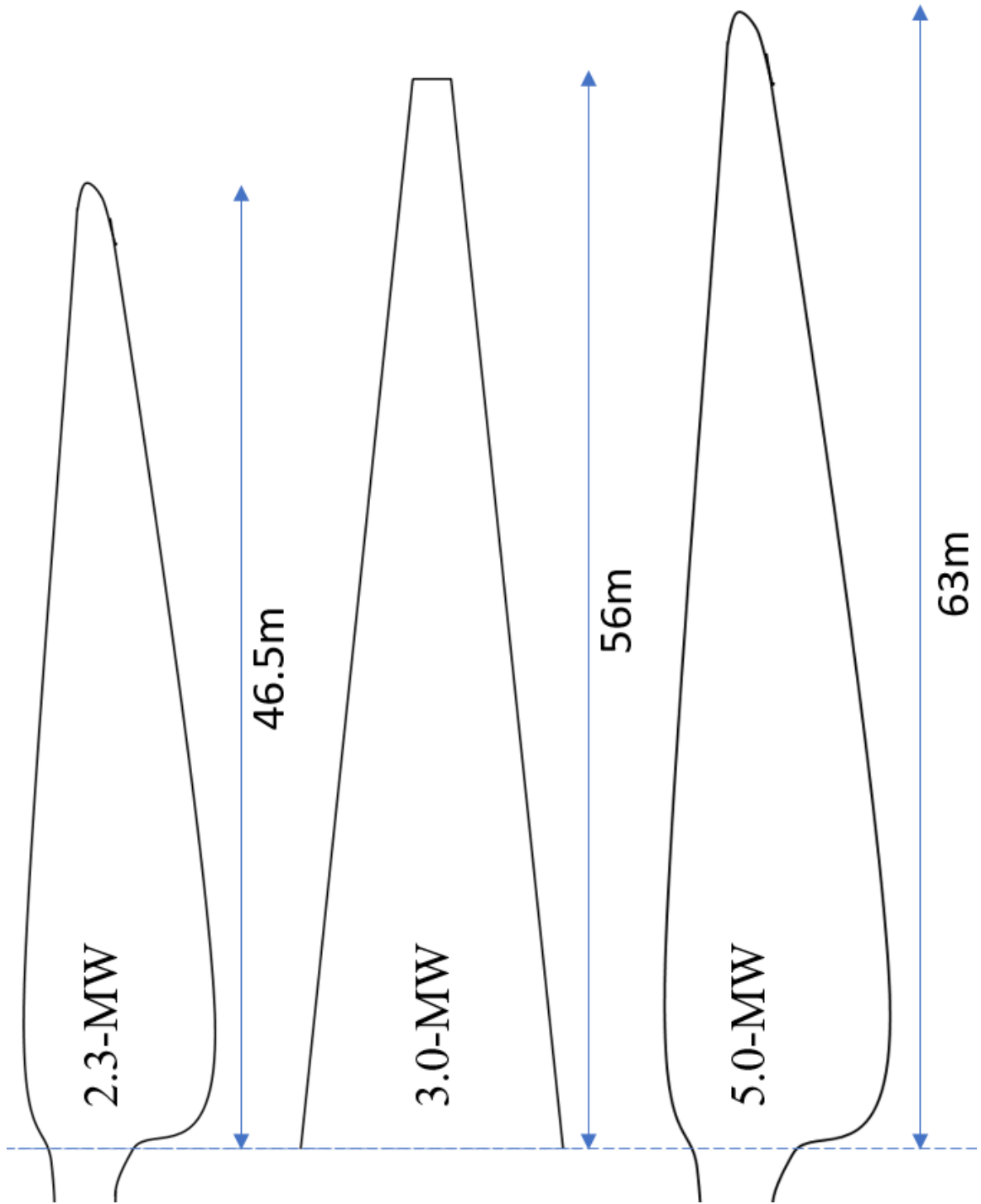


**Figure 1.3:** Schematic of the blades of three wind turbines: Siemens SWT-2.3-93, Vestas V112-3.0, and NREL-5MW.

Blade Element	Radius (m)	Twist ( $^{\circ}$ )	Length (m)	Chord (m)	Airfoil
1	2.8667	13.308	2.7333	3.542	Cylinder1
2	5.6000	13.308	2.7333	3.854	Cylinder1
3	8.3333	13.308	2.7333	4.167	Cylinder2
4	11.7500	13.308	4.1000	4.557	DU40_A17
5	15.8500	11.480	4.1000	4.652	DU35_A17
6	19.9500	10.162	4.1000	4.458	DU35_A17
7	24.0500	9.011	4.1000	4.249	DU30_A17
8	28.1500	7.795	4.1000	4.007	DU25_A17
9	32.2500	6.544	4.1000	3.748	DU25_A17
10	36.3500	5.361	4.1000	3.502	DU21_A17
11	40.4500	4.188	4.1000	3.256	DU21_A17
12	44.5500	3.125	4.1000	3.010	NACA64_A17
13	48.6500	2.319	4.1000	2.764	NACA64_A17
14	52.7500	1.562	4.1000	2.518	NACA64_A17
15	56.1667	0.863	2.7333	2.313	NACA64_A17
16	58.9000	0.370	2.7333	2.086	NACA64_A17
17	61.6333	0.106	2.7333	1.419	NACA64_A17

**Table 1.1:** Aerodynamic properties of the NREL-5MW wind turbine based on incompressible blade element theory.

Blade Element	Radius (m)	Twist ( $^{\circ}$ )	Length (m)	Chord (m)	Airfoil
1	2.5714	9.000	2.1430	2.036	Cylinder1
2	4.7143	9.000	2.1430	2.065	Cylinder2
3	6.8571	9.000	2.1430	2.334	Cylinder2
4	9.0000	9.000	2.1430	2.736	FFA_W3-301
5	11.1429	9.000	2.1430	3.137	FFA_W3-301
6	13.2857	9.000	2.1430	3.485	FFA_W3-301
7	15.4286	9.000	2.1430	3.372	FFA_W3-301
8	17.5714	9.000	2.1430	3.183	FFA_W3-301
9	19.7143	8.079	2.1430	2.995	FFA_W3-241
10	21.8571	6.014	2.1430	2.807	FFA_W3-241
11	24.0000	4.231	2.1430	2.618	FFA_W3-241
12	26.1429	2.589	2.1430	2.430	FFA_W3-211
13	28.2857	1.303	2.1430	2.242	FFA_W3-211
14	30.4286	0.281	2.1430	2.054	NACA_63-221
15	32.5714	-0.594	2.1430	1.865	NACA_63-221
16	34.7143	-1.303	2.1430	1.677	NACA_63-218
17	36.8571	-1.840	2.1430	1.489	NACA_63-218
18	39.0000	-2.274	2.1430	1.300	NACA_63-218
19	41.1429	-2.627	2.1430	1.112	NACA_63-218
20	43.2857	-2.842	2.1430	0.924	NACA_63-218
21	45.4286	-2.973	2.1430	0.735	NACA_63-218

**Table 1.2:** Aerodynamic properties of the Siemens SWT-2.3-93 wind turbine based on incompressible blade element theory.

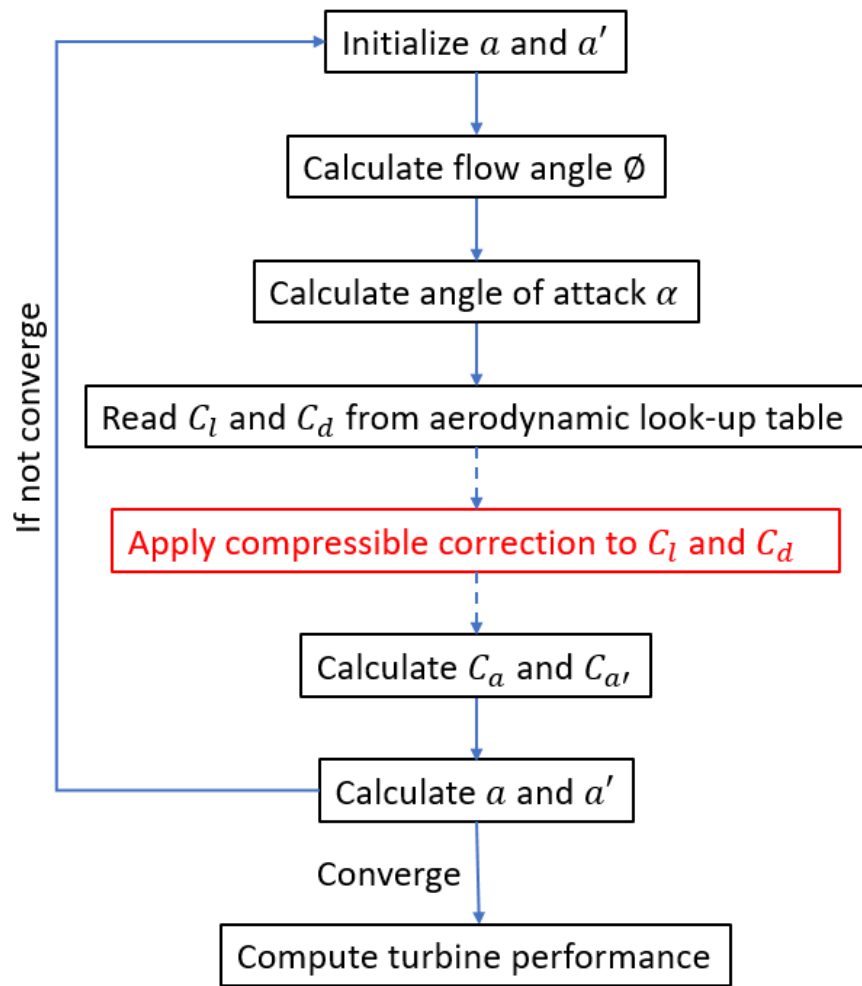


**Figure 1.4:** Algorithm for incompressible BEM (without the red block) and compressible corrected BEM (with the red block).

total thrust (Eq. 1.13); a decrease in the power coefficient (Fig. 1.5a) and in the total torque (Eq. 1.14); and ultimately a decrease in the power generated (Fig. 1.5c).

The well-designed Siemens SWT-2.3-93 shows a very similar behavior as the NREL-5MW, with the optimum operating TSR around 8 (Fig. 1.6(a)). Compressibility effects are barely noticeable for all different incoming wind speeds when TSR is smaller than 10. As TSR increases, for incoming wind speeds of 5 and 10 m s<sup>-1</sup>, the compressibility effects still remain small even for the largest TSR. However, for wind speeds above 15 m s<sup>-1</sup>, compressibility effects can be important and the turbine performance is degraded for TSR larger than 12. An increase in the thrust coefficient (Fig. 1.6b) and in the total thrust is also observed, due to the way they are calculated.

The efficiency of the linearly designed Vestas V112-3.0, on the other hand, is not as good as the previous two wind turbines. The optimal operating TSR is around 11 with a lower maximum  $C_p$  (Fig. 1.7a). The turbine performance is only degraded for the highest incoming wind speed (20 m s<sup>-1</sup>) and the largest TSR (>14). Contrarily to the other two turbines, compressibility effects slightly boost the performance of the wind turbine for TSR around the optimal value of 11. This is because the forces along the rotor plane are calculated as  $L \sin \phi - D \cos \phi$  (Fig. 1.2b) and the Prandtl-Glauert compressibility corrections increase both lift and drag as Mach number increases, thus for the simply designed Vestas V112-3.0, the boost of performance is more obvious than for the Siemens SWT-2.3-93.

### 1.2.5 Conclusions

In this study, compressibility effects on the blade aerodynamic coefficients are assessed for three large horizontal-axis wind turbines. Different turbine blade designs respond differently to the compressibility effects. Under normal operating conditions, the compressibility effects either will not affect the power production or slightly alter it in a positive way; only for extreme operating conditions, compressibility effects will significantly degrade the performance of the wind turbines.

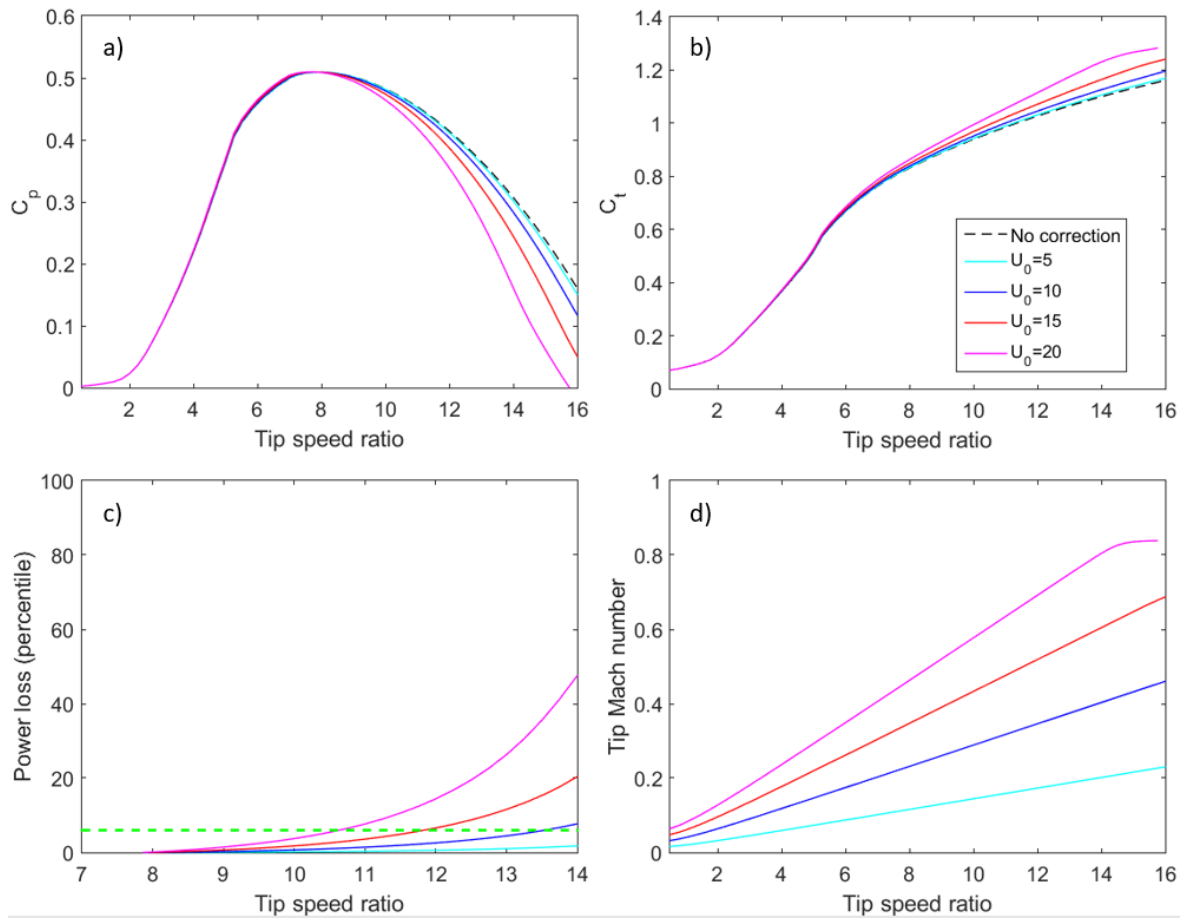


**Figure 1.5:** Effects of compressibility correction: a) power coefficient  $C_p$ , b) thrust coefficient  $C_t$ , c) power loss (%) and d) tip Mach number as a function of the tip speed ratio for the NREL-5MW wind turbine.

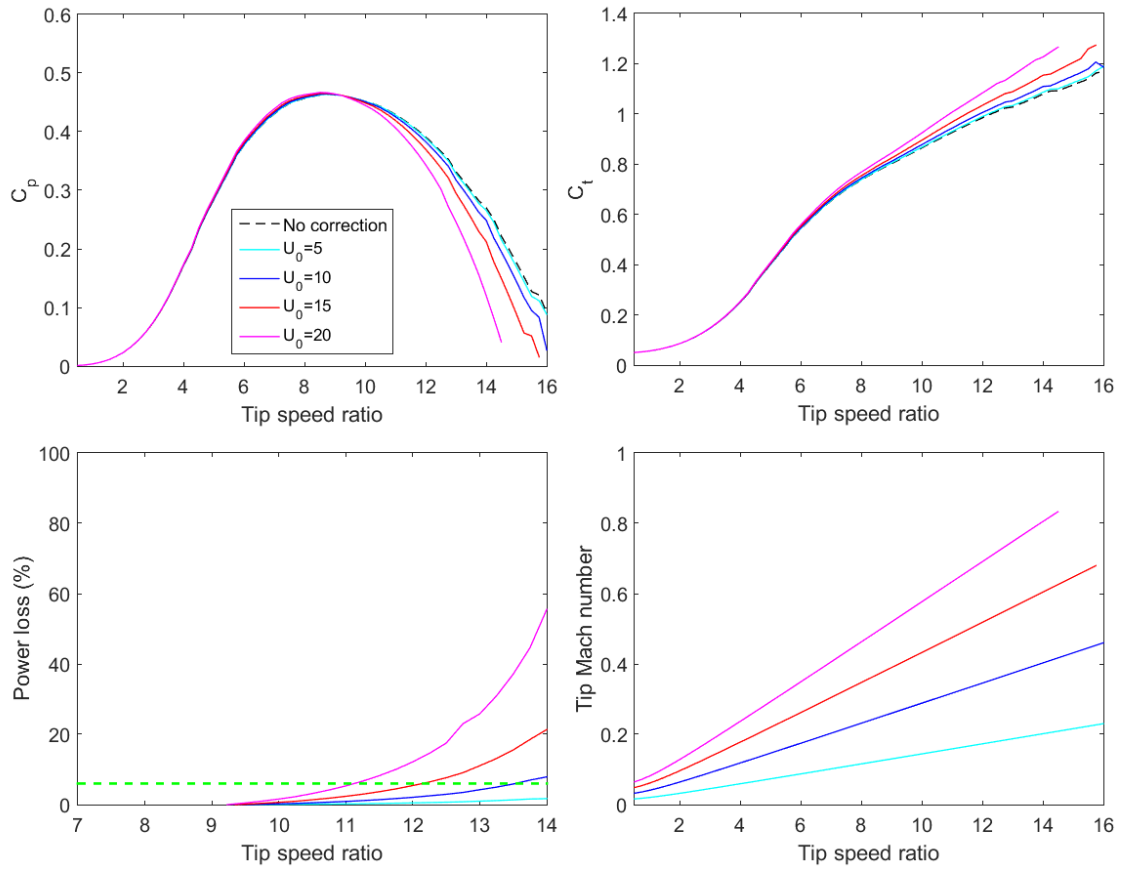


**Figure 1.6:** Effects of compressibility correction: a) power coefficient  $C_p$ , b) thrust coefficient  $C_t$ , c) power loss (%) and d) tip Mach number as a function of the tip speed ratio for the Siemens SWT-2.3-93 wind turbine.

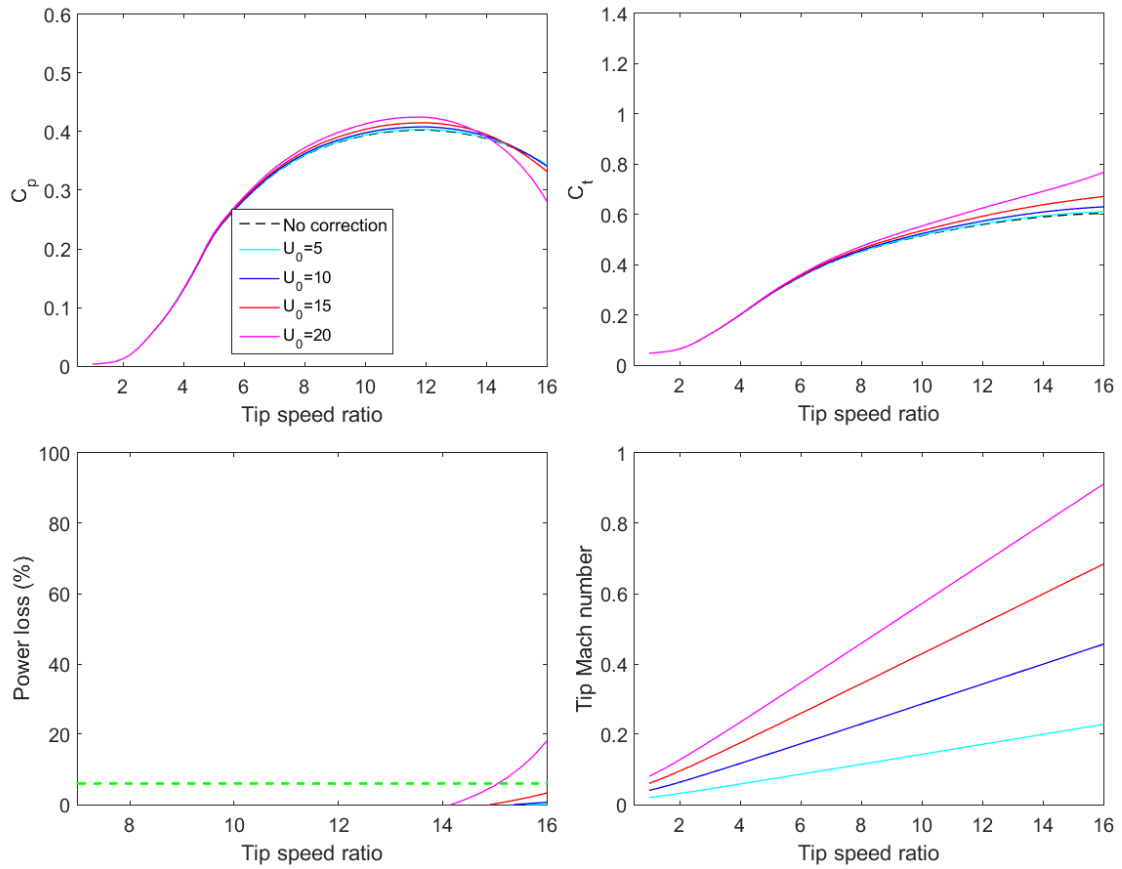


**Figure 1.7:** Effects of compressibility correction: a) power coefficient  $C_p$ , b) thrust coefficient  $C_t$ , c) power loss (%) and d) tip Mach number as a function of the tip speed ratio for the Vestas V112-3.0 wind turbine.

In real-world wind farms, the operating TSRs are always kept around the optimum value, which is around 8 in general and rarely greater than 12 for large horizontal-axis wind turbines. In addition, the incoming wind speeds, even for the front-row turbines, are rarely above  $15 \text{ m s}^{-1}$ . When encountering severe operating conditions, such as hurricanes or tornadoes, the wind turbines will simply be shut down. Thus we conclude that it is acceptable to use the provided incompressible aerodynamic coefficients to model the power production of large wind turbines and that compressibility effects on aerodynamic properties are negligible under normal operating conditions.

### 1.3 Compressibility effects on air density

Other than the aerodynamic coefficients of the turbine blades, the incompressible assumption is also questionable on air density. A typical averaged or filtered (or  $\sim$  sign is omitted) governing momentum equation for wind turbine modeling is:

$$\frac{\partial u_i}{\partial t} + u_j \frac{\partial u_i}{\partial u_j} = -\frac{\partial p}{\partial x_i} - \frac{\partial \tau_{tij}}{\partial x_j} + B + C + f_i \quad (1.18)$$

where  $p$  is the modified pressure,  $\tau_{tij}$  is the turbulent shear stress,  $B$  is the buoyancy term,  $C$  is the Coriolis force,  $f_i$  is the turbine induced force and all other terms have their traditional forms. In the real atmosphere, air density slowly decreases with height. This buoyancy effect is accounted for by using the Boussinesq approximation. However, the turbine induced force  $f_i$  is a density-normalized force. When using the BEM method, ADM, or ALM to model the turbine performance, the real forces (torque, thrust) are calculated as the density-normalized force multiplied by a constant reference density, thus the choosing of this constant density needs special attention. Sometimes, the density near the ground level is used; sometimes, the hub height density is used; a more accurate choice would be using the rotor-disk averaged density. Using different air densities will cause a direct change in the power prediction, for example, using  $1.25 \text{ Kg m}^{-3}$  instead of  $1.2 \text{ Kg m}^{-3}$  will cause a direct increase in power of 4.2%, which is not a small difference in terms of power prediction.

Except for the vertical variance, air density will also be altered by compressibility effects near the turbine tip region because air flow near that region can become subsonic, thus air density will change due to high pressure. The incompressible BEM method, ADM, ALM cannot deal with this problem, unless a compressible framework is used.

Variable density effects can cause a direct change on turbine power production as well as on the flow field. In this section, we conduct assessments of the variable-density effects by performing all simulations using both the incompressible and the compressible framework. Differences between the simulation results using both frameworks are presented in order to highlight the effects clearly.

### 1.3.1 Numerical methods

For the incompressible Boussinesq framework (“Incomp” hereafter), we adopt the open-source package SOWFA (Simulator for On/Offshore Wind Farm Applications) (Churchfield et al., 2012a,b), which was developed at the U.S. Department of Energy’s NREL based on OpenFOAM (Open source Field Operation And Manipulation), a set of open-source C++ libraries for the development of customized numerical solvers. SOWFA is well established and validated for wind farm applications (Archer et al., 2013; Ghaisas et al., 2017; Bhaganagar and Debnath, 2015). Turbines in SOWFA are modeled using ALM, but the nacelle and tower of the turbines are not modeled. The governing equations used in SOWFA were discussed in Section 1.

For the compressible framework (“Comp” hereafter), in order to maintain high consistency with the incompressible framework and make the results between the two frameworks comparable, we follow the procedure of SOWFA and develop our solver based on OpenFOAM, thus turbines are modeled using ALM (Fig. 1.1b). While assessing the variable-density effects, we want to exclude the aerodynamic effects, thus the tabulated lift and drag coefficients of the blade airfoils are kept identical in both solvers. This is consistent with the findings in Section 1.2.1 that compressibility effects are negligible on aerodynamic properties of wind turbines operating under normal flow and TSR conditions. The governing equations in the compressible framework are the Favre-averaged continuity, momentum, and enthalpy equations:

$$\frac{\partial \bar{\rho}}{\partial t} + \frac{\partial}{\partial x_i} (\bar{\rho} \tilde{u}_i) = 0, \quad (1.19)$$

$$\frac{\partial}{\partial t} (\bar{\rho} \tilde{u}_i) + \frac{\partial}{\partial x_j} (\bar{\rho} \tilde{u}_j \tilde{u}_i) = -\frac{\partial \bar{p}}{\partial x_i} + \frac{\partial}{\partial x_j} (\tau_{ij} + \tau_{t_{ij}}) + \bar{\rho} g_i + \bar{\rho} f_i, \quad (1.20)$$

$$\frac{\partial}{\partial t} (\bar{\rho} \tilde{h}) + \frac{\partial}{\partial x_j} (\bar{\rho} \tilde{u}_j \tilde{h}) = \frac{\partial \bar{p}}{\partial t} - \frac{\partial \tilde{Q}_j}{\partial x_j} - \frac{\partial \tilde{Q}_{t_j}}{\partial x_j}, \quad (1.21)$$

$$\bar{p} = \bar{\rho} R \tilde{T}, \quad (1.22)$$

where  $\tilde{u}_i = \overline{\rho u_i} / \bar{\rho}$  and  $\tilde{h} = \overline{\rho h} / \bar{\rho}$  are the Favre-averaged velocity and enthalpy, the laminar stress tensor  $\tau_{ij} = \mu \left[ \left( \frac{\partial \tilde{u}_i}{\partial x_j} + \frac{\partial \tilde{u}_j}{\partial x_i} \right) - \frac{2}{3} \left( \frac{\partial \tilde{u}_k}{\partial x_k} \right) \delta_{ij} \right]$  and heat flux  $Q_j = -\frac{\mu}{Pr} \frac{\partial \tilde{h}}{\partial x_j}$ . The turbulent stress tensor, split into a deviatoric and an isotropic part, by adopting the eddy-viscosity hypothesis for the deviatoric part, can be calculated as:

$$\tau_{t_{ij}} = \mu_t \left[ \left( \frac{\partial \tilde{u}_i}{\partial x_j} + \frac{\partial \tilde{u}_j}{\partial x_i} \right) - \frac{2}{3} \left( \frac{\partial \tilde{u}_k}{\partial x_k} \right) \delta_{ij} \right] - \frac{1}{3} \tau_{kk} \delta_{ij}, \quad (1.23)$$

where  $\mu_t$  is the turbulent viscosity, calculated with the  $k - \varepsilon$  equations (Launder and Spalding, 1974). The turbulent heat flux, with the eddy-viscosity hypothesis, is calculated as:

$$Q_{t_j} = -\frac{\mu_t}{Pr_t} \frac{\partial \tilde{h}}{\partial x_j}, \quad (1.24)$$

where  $Pr_t$  is the turbulent Prandtl number. Again, the purpose of this section is to discover the variable-density compressibility effects alone, thus high consistency is required between the two frameworks. Because the standard  $k - \varepsilon$  model (Launder and Spalding, 1974) is highly consistent between the two, it was chosen in this study as the turbulence closure for the governing equations. The compressible form has been used with success in variable-density thermal stratified flow (Khalil et al., 1975) and free shear flows with Mach number effects (Launder et al., 1973).

Both the incompressible and compressible governing equations are discretized using the finite volume method on unstructured meshes. All variables are cell-centered and collocated on the grid. Linear interpolation (equal to second-order central differencing) is used to interpolate cell-centered variables to cell faces. The system of equations is solved using the predictor-corrector Pressure Implicit Splitting Operation (PISO) method (Issa, 1986) and the implicit terms are integrated in time using Crank-Nicolson discretization; one predictor with two correctors are used in this study. The discretized momentum and enthalpy/temperature equations are solved using an iterative diagonal incomplete-LU preconditioned bi-conjugate gradient matrix solver; the discretized pressure equations are solved using an iterative preconditioned conjugate gradient solver with a diagonal incomplete Cholesky smoother. Both the incompressible and compressible codes are parallelized using the message-passing interface (MPI).

All simulations of this study are conducted on a high-performance computing cluster with 192 processors.

The differences between the two frameworks will be always discussed as “Comp minus Incomp”, where Incomp is taken as the reference.

### 1.3.2 Single wind turbine cases

This section explores the compressibility effects associated with variable density in the flow field around a single NREL-5MW wind turbine operating in the ABL. The simulations were carried out in a Cartesian computational domain with streamwise, spanwise, and vertical lengths of 3024, 756, and 756 m, respectively. Using the diameter of the NREL 5MW wind turbine as reference ( $D=126$  m), the domain size can be expressed in non-dimensional form as  $24D \times 6D \times 6D$  (Fig. 1.8a). The computational domain is evenly divided in each direction into  $N_x \times N_y \times N_z = 312 \times 144 \times 144$  grid points of sizes  $\Delta x \times \Delta y \times \Delta z = 9.7 \text{ m} \times 5.25 \text{ m} \times 5.25 \text{ m}$ .

A constant geostrophic wind speed  $U_g$  is imposed at the domain top and periodic boundary conditions are used at the spanwise and streamwise boundaries, so that the two frameworks simulate an infinitely-large atmospheric boundary layer. The Reynolds number is sufficiently high to neglect molecular viscosity, except at the first grid point off the ground, where the Schumann’s wall model is imposed (Schumann, 1975) and the roughness length is set to be  $z_0=0.016$  m. The simulations are carried out first for the ABL without wind turbines for 14400 seconds (physical time), which is long enough for turbulence to become fully developed to capture the log-law of the ABL (precursor run). Then we collect the flow information at the inflow boundaries from 7200 to 14400 s and start the new simulations with the addition of the wind turbine and the inflow boundary conditions from the precursor run. The turbine is located  $3D$  downstream from the inlet section and at the center in the spanwise direction. The height of the turbine hub is 87.6 m (or  $0.7D$ ). The actuator lines rotate counter-clockwise in the x-plane. For the simulations with wind turbine, periodic conditions are used at the spanwise boundaries and the free-slip condition is used at the top. Since at the inlet

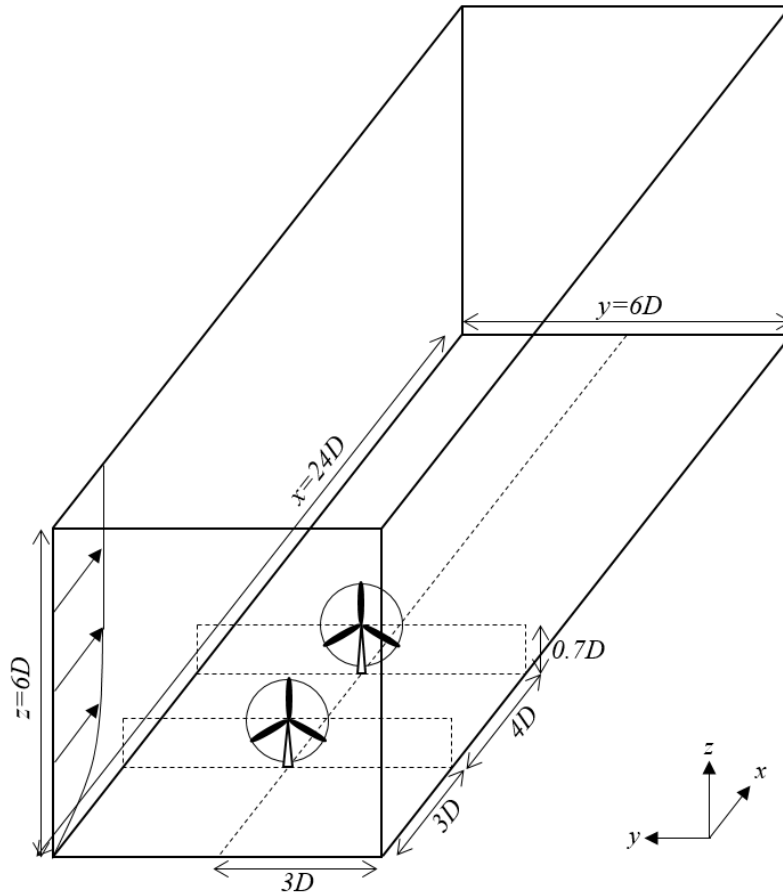


**Figure 1.8:** Schematic of the computational domain (not to scale) for the single-turbine and two-turbine cases. Domain sizes are expressed as multiples of the diameter of the reference NREL 5-MW wind turbine ( $D=126$  m). The circles represent the turbine rotors.

section in the streamwise direction of the domain the inflow information comes from the “precursor” simulation, the inflow is effectively non-periodic and unaffected by the wake of the wind turbine. At the outlet, a zero-gradient condition is imposed. Details of the simulations are provided in Table 1.3.

Case	N. turbines	$U_g$ m s <sup>-1</sup>	$U_{hub}$ m s <sup>-1</sup>	$\Omega_1$ rpm	$\Omega_2$ rpm	TSR
1	1	15	11.83	10		5.58
2 (Control)	1	15	11.83	15		8.37
3	1	10	7.88	10		8.37
4	1	10	7.88	15		12.56
5	2	15	11.83	15	10	8.37

**Table 1.3:** Setup of the five cases considered, with different geostrophic and hub-height wind speeds ( $U_g$  and  $U_{hub}$ ), rotational speed  $\Omega$ , and tip speed ratio (TSR). The TSR value for Case 5 is for the front-row turbine only.

The first variable of interest is wind speed, shown in Fig. 1.9 for the control case (Case 2 in Table 1.3). In both compressible and incompressible simulations, the flow decelerates in front of the turbine while accelerating in the region enveloping the wake. The acceleration in the outer wake, also found in previous studies (Ghaisas and Archer, 2016; Ghaisas et al., 2017), vanishes quickly around 2D downstream of the wind turbine. This acceleration is slightly lower in Comp than in Incomp, thus Fig. 1.9c shows wings of negative wind speed differences outside of the rotor circle (light blue in 1.9c). Similarly, the deceleration of the flow right in front of the turbine is stronger in Comp and therefore the wind speed right in front of the rotor is slightly weaker with Comp than with Incomp ( $\sim 0.2$  m s<sup>-1</sup> in Fig. 1.9c).

In the wake, the wind speed simulated by Comp is slightly higher than that in Incomp, or the wind speed deficit is slightly weaker in the Comp than Incomp results, thus the positive wind speed difference in Fig. 1.9c. The difference caused by compressibility effects has a typical “bowl” shape, reaches its maximum in the near-wake region ( $\sim 0.3$  m s<sup>-1</sup>) by 3D, and becomes negligible in the far-wake region.

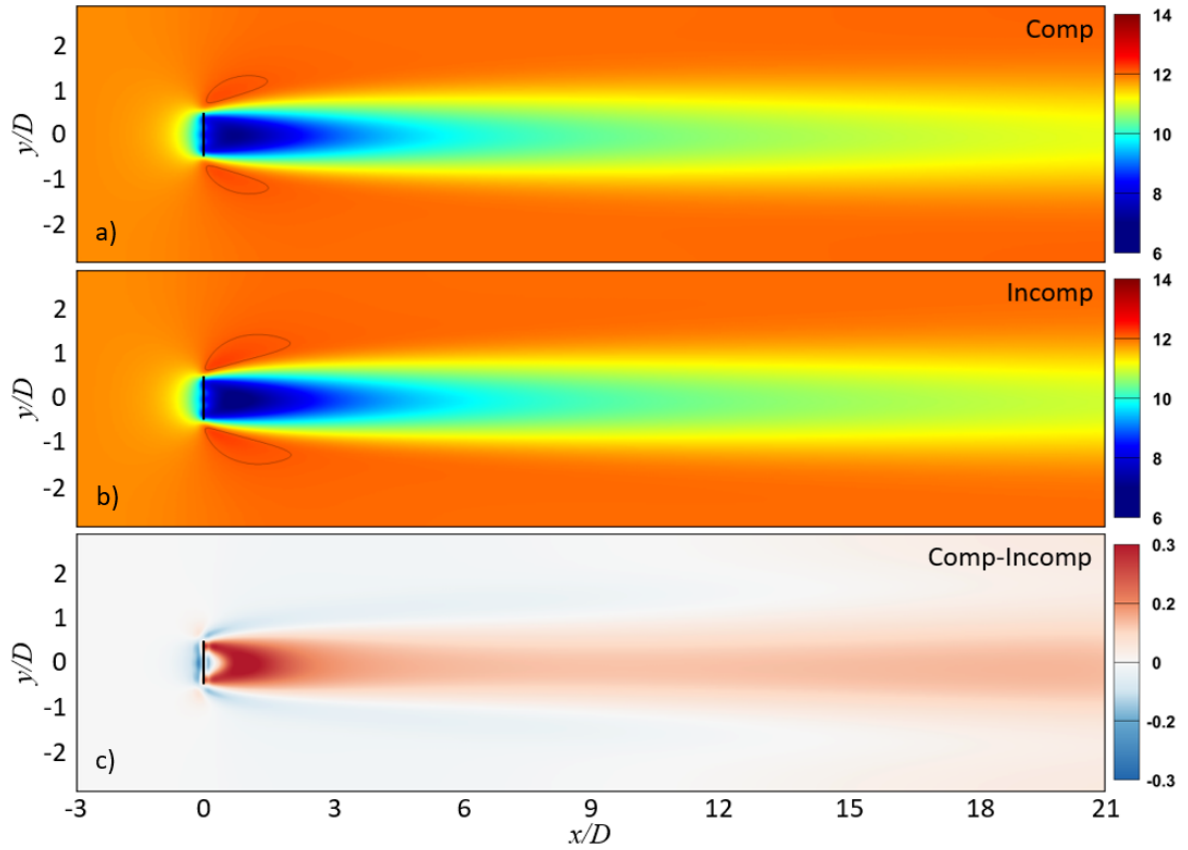


**Figure 1.9:** Case 2: Horizontal cross-sections at hub height of: a) Comp wind speed, b) Incomp wind speed, and c) Comp - Incomp wind speed difference, all in  $\text{m s}^{-1}$ . The  $12 \text{ m s}^{-1}$  contour line is shown in black in a) and b).

The differences can be explained by comparing the two frameworks phenomenologically. In incompressible flow, when a volume of air hits the blades, no energy is used to compress the air volume and all of it is used to push the blades and deflect the air. In compressible flow, a small fraction of the kinetic energy is used to slightly compress the air, thus the wind speed is lower in front of the rotor, the power extracted is less, and the speed in the wake is higher.

Vertical and horizontal profiles of wind speed (Fig. 1.10) for both frameworks confirm the previous findings. In general, the wind speed deficit is slightly weaker in the Comp wake starting at 1D, but it is almost recovered to the Incomp value by 5D (Fig. 1.10b). The shape of the horizontal TKE distribution is similar in the two frameworks, with two peaks at the left and right tips of the rotor, which merge into one at 3D (Fig. 1.11b). The Comp wake has always smaller values of TKE than the Incomp wake, by up to  $\sim 15\%$ , which is counter-intuitive in a wake with higher wind speed (Archer et al., 2016). In incompressible flow, fluctuations in velocity that contribute to TKE are stronger because no energy is used to compress the air, whereas in compressible flow the perturbations are slightly damped because some energy is used towards density changes. In the vertical, again, the wakes simulated by the two frameworks have similar TKE shapes with a strong peak at the top tip of the rotor and a weaker peak at the bottom tip (Fig. 1.11a), as found also in previous studies (Xie and Archer, 2015), but the Comp TKE is lower than the Incomp TKE by up to 10%.

Going back to the rule-of-thumb for incompressible flow, any increase in the flow velocity would increase the Mach number and therefore increase the compressibility effects. Two properties that would increase the flow velocity are the hub-height wind speed ( $U_{hub}$ ) and the rate of rotation of the turbine  $\Omega$ , both of which have been found to influence the wind speed deficit and the turbulence properties of wind turbine wakes (Vermeer et al., 2003; Hansen et al., 2006; Sanderse et al., 2011; Sørensen, 2011). The

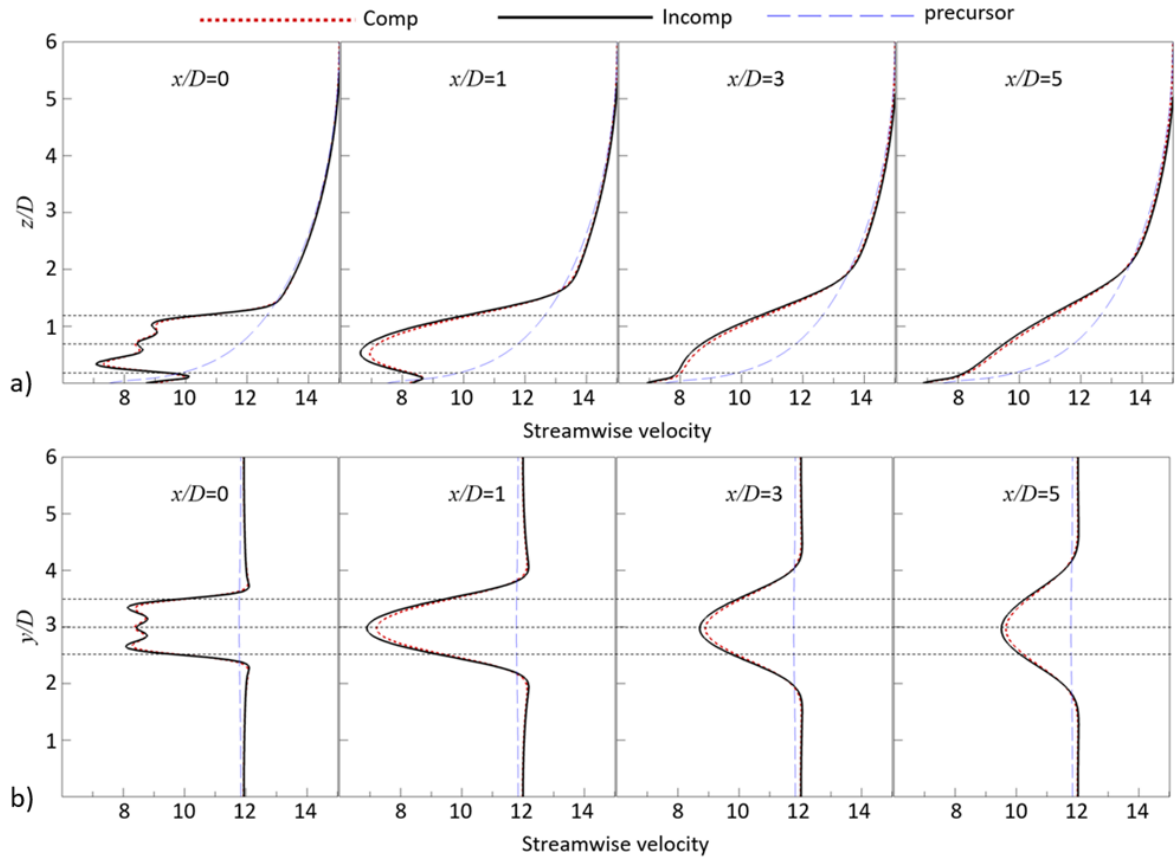


**Figure 1.10:** Case 2: Vertical (a) and lateral (b) profiles of wind speed ( $\text{m s}^{-1}$ ) along the wake centerline at various distances downstream of the turbine (expressed as multiples of the turbine diameter  $D$ ). The black dashed lines represent positions of the turbine hub and tips.

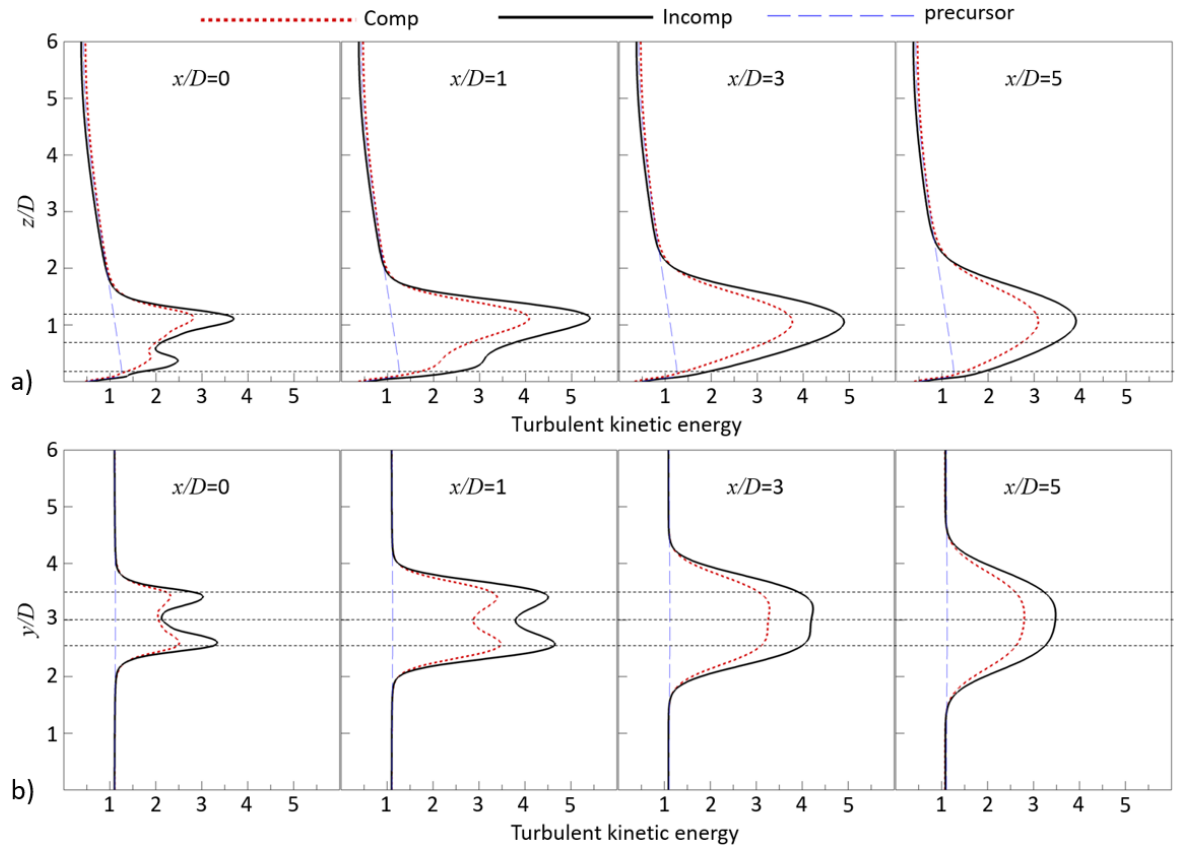


**Figure 1.11:** Case 2: a) vertical and b) lateral profiles of TKE ( $\text{m}^2 \text{s}^{-2}$ ) along the wake centerline at various distances downstream of the turbine (expressed as multiples of the turbine diameter  $D$ ). The black dashed lines represent positions of the turbine hub and tips.

two properties are combined in the TSR:

$$TSR = \frac{\Omega R}{U_{hub}}. \quad (1.25)$$

The sensitivity of Comp and Incomp results to both is analyzed here, for increasing values of the TSR (corresponding to Cases 1, 2, 3 and 4 in Table 1.3).

Compressibility effects begin near the tip region, but are not confined there, as wind speed differences are found in the wake with the “bowl” shape in all cases (Fig. 1.12, left). An increase of the magnitude of the wind speed differences is observed as TSR increases. For Case 1 with the lowest TSR, the largest difference is around 1%; for Case 2 and 3 with the same TSR, the largest difference is around 2%; for Case 4 with the highest TSR, the difference is up to 3%. Another finding is that the shape of the affected region is also related to TSR. For low TSR, which means relatively high free-stream wind speed, the affected region extends all the way to the far wake without a significant decay in the magnitude of the wind speed difference (Fig. 1.12, top); for intermediate TSR, the affected region still extends to the far-wake region, but with a decay in the magnitude (Fig. 1.12, middle); for high TSR, which means relatively low free-stream wind speed, the affected region is confined to the near-wake and becomes negligible in the far wake (Fig. 1.12, bottom).

Compressibility also changes the turbulence properties of the wake (Fig. 1.12, right). Bowl-shaped TKE differences are again observed in the near-wake region, since the TKE differences also origin from the high Mach number zone, i.e., the turbine tip circle region, and then the region further downstream is affected. The Comp wake always exhibits less TKE than the Incomp, thus the negative value of TKE differences. Both the magnitude and the extent of the TKE differences increase with TSR; however, for all TSRs, the TKE differences disappear past 10D.

Figure 1.13 shows the cross-sections in the rotor plane of Comp minus Incomp wind speed differences for different TSR. The blue rings are caused by the different accelerations outside of the rotor circle, as observed in Fig. 1.9c. The red rings are the origin of the bowl-shaped wind speed differences near the tips of the blades and

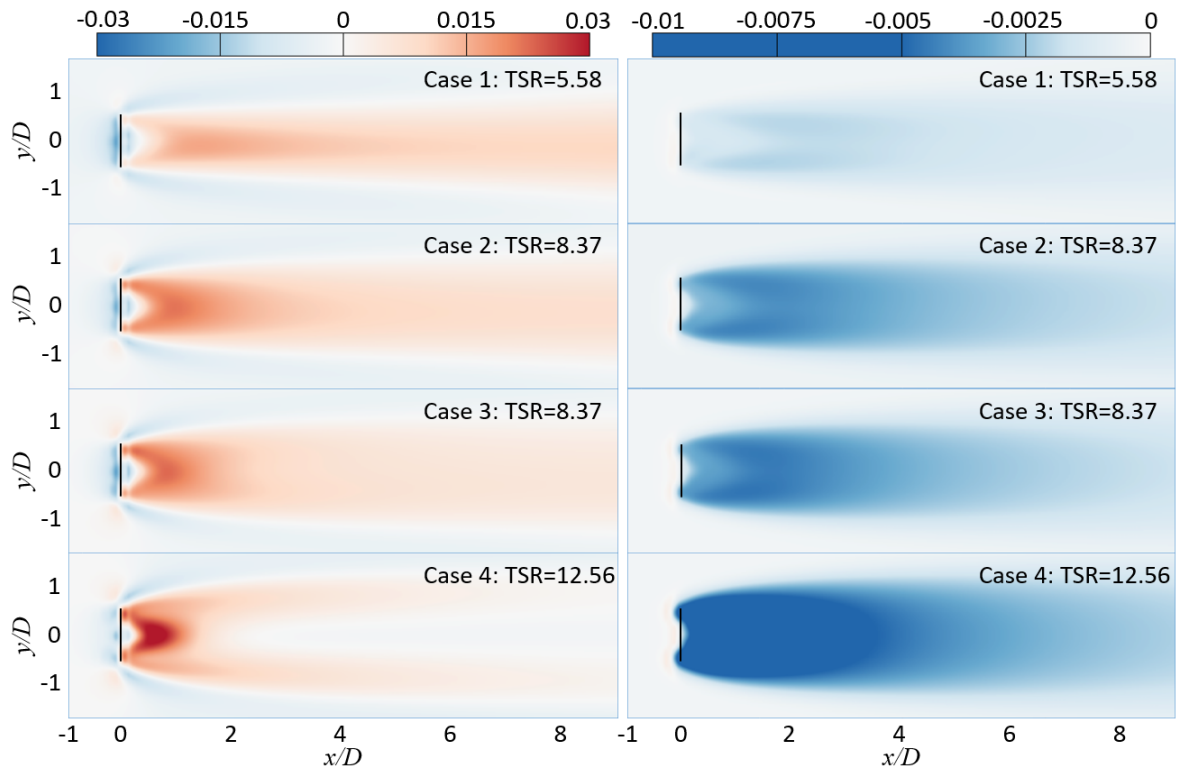


**Figure 1.12:** Horizontal cross-sections of Comp - Incomp wind speed difference (left) and Comp - Incomp TKE difference (right) at hub height, normalized by  $U_{hub}$  and  $U_{hub}^2$  respectively, for the four single-turbine cases in Table 1.3.

the change of their magnitude is consistent with previous findings, with higher TSR corresponding to larger differences between the two frameworks. These figures show that the compressibility effects originate at the rotor tips.

Last, the effects on wind power production is discussed. Compressibility effects related to variable density show up as a slightly degraded turbine performance (Fig. 1.14a) and they increase with TSR (Fig. 1.14b, circles). For Case 1, with a TSR of 5.58, the power coefficient decreases by about 3% from Incomp to Comp; for Case 2 and 3 (TSR=8.37) by about 8% (note that the two cases are indistinguishable in the figure); and for Case 4 (TSR=12.56) by 20%. Although these values from compressible and incompressible simulations are not directly comparable with the theoretical curves shown in Fig. 1.5, which were obtained using blade element theory for a uniform incoming wind speed, we put them together in Fig. 1.14b. The two compressibility effects: on aerodynamic properties (solid and dashed curves) and on air density (circles and filled circles), have a similar pattern, meaning that both cause power to be reduced switching from incompressible to compressible and more so for high TSRs, although the variable-density effect is larger.

Several conclusions can be drawn already from the single-turbine case. First, compressibility effects are not negligible and are not limited to the region near the blade tips, but impact the entire wake. The magnitude and extent of the effects in the wake depend on the tip speed ratio. A wind turbine wake has a weaker wind speed deficit, higher wind speed and lower turbulence in the wake, and produces less power when compressibility effects are taken into account than when they are ignored. Since most wind farms include more than a single turbine, it is important to verify if and how these effects come to play when multiple turbine wakes interact with each other, as they do in a wind farm. This issue will be addressed in the next section.

### 1.3.3 Two aligned wind turbines

This section explores the compressibility effects in the flow field of two NREL 5-MW wind turbines operating in the same ABL flow discussed in the previous section.

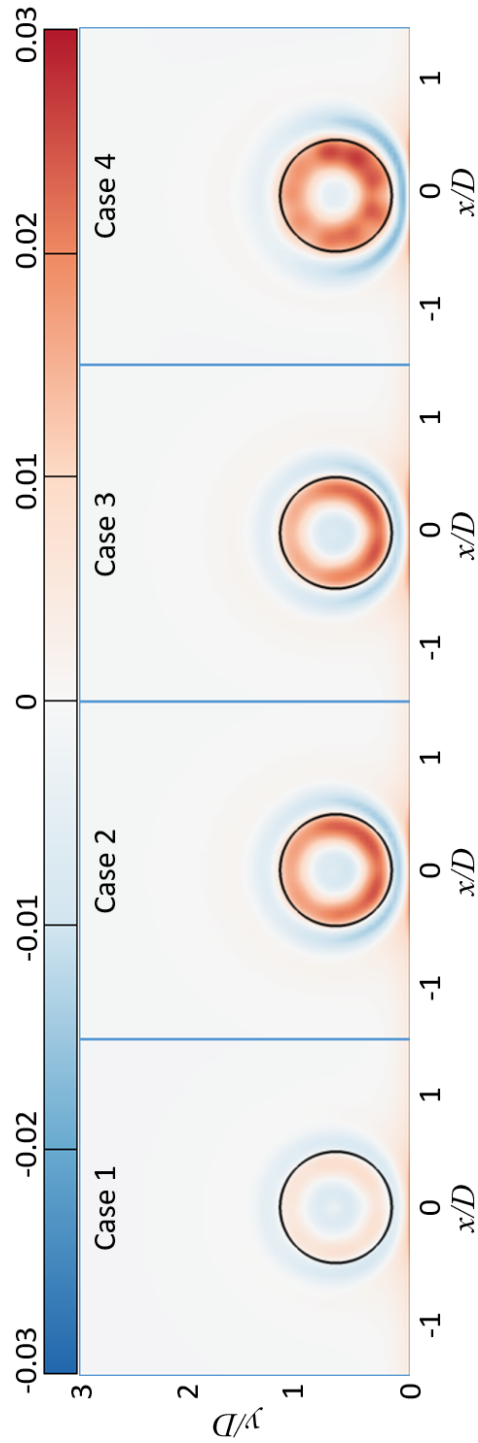


**Figure 1.13:** Vertical cross-sections in the rotor plane of Comp - Incomp wind speed difference, normalized by  $U_{hub}$ , for the four single-turbine cases in Table 1.3.

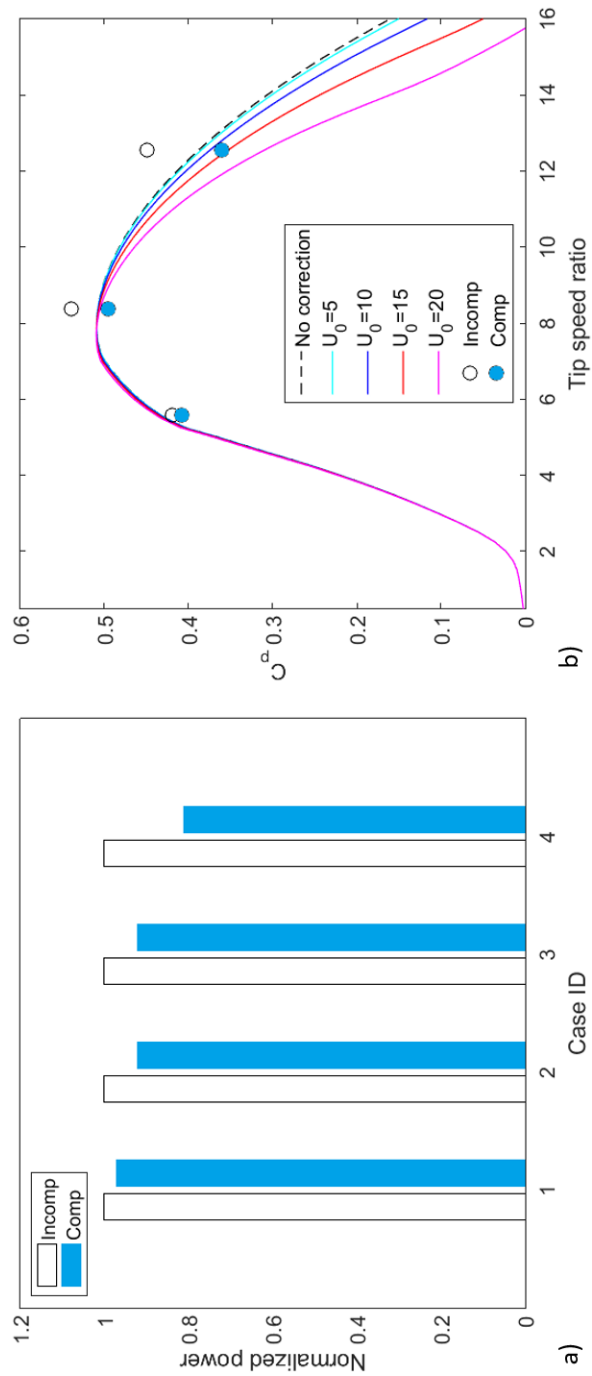


**Figure 1.14:** a) Power production of the four incompressible and four compressible single-turbine cases described in Table 1.3, normalized by the power of the incompressible cases. b) Effects of compressibility on the power coefficient  $C_p$  from BEM (lines) and Comp/Incomp simulations (circles).

The numerical setup for two turbine simulations is kept the same as the single turbine simulations, the only difference is that now we have two wind turbines aligned, one located at  $x=3D$  and the other one at  $x=7D$ , which are  $4D$  apart (Fig. 1.8b). The rotational speed of the first and second turbine is 15 and 10 rpm, respectively (Table 1.3).

The general behaviour of the wind speed difference for the front-row turbine is similar to the single-turbine case, i.e., a weaker wind speed deficit (indicated by the positive wind speed differences within the rotor area in Fig. 1.15a), weaker acceleration outside of the rotor area, and lower TKE (Fig. 1.15b) with Comp than with Incomp. In overlapping wakes, some compressibility effects are enhanced and some are damped. TKE differences are enhanced, meaning that the Comp flow field becomes less and less turbulent than the Incomp flow field past two or more turbines. On the other hand, wind speed differences are damped, with a similar bowl-shaped pattern as in the control case, but generally weaker and less extended downstream past the second turbine. This suggests that, without considering TKE, wind power production is most different at the front row, with Incomp predicting higher power than Comp, but the two converge eventually as the number of turbines downwind increases.

Horizontal profiles of wind speed and TKE for both frameworks (Fig. 1.16) confirm that wind speed and TKE respond differently in overlapping wakes when compressibility effects are considered. The wind speed deficit difference becomes insignificant at the second turbine and remains as such downstream. TKE is higher in the second wake with both frameworks, but the TKE difference becomes even larger past the second turbine than past the first.

#### 1.3.4 Validation

To validate the results, we acquired power production data at an existing wind farm, the Lillgrund offshore wind farm (Archer et al., 2013), located off the coast of Sweden in the Baltic Sea, for a period of approximately three years at a temporal resolution of 1 minute. Lillgrund contains 48 Siemens SWT-2.3MW wind turbines

(Siemens AG, 2009) with rotor diameter  $D = 93$  m and hub height  $H = 63.4$  m. The prevailing wind direction at Lillgrund is from the southwest ( $225^\circ$ ), for which the turbine spacing is  $4.3D$  along the wind and  $3.2D$  across the wind, similar to the spacing used in the previous sections.

We conducted a simulation of the entire Lillgrund wind farm using the compressible framework with the aim of comparing the simulated power output against the observed to validate the results. The computational domain has streamwise, spanwise, and vertical lengths of 4000, 4000, and 756 m, respectively (Fig. 1.17a). The computational domain is divided in each direction into  $N_x \times N_y \times N_z = 512 \times 512 \times 144 = 37,748,736$  grid points of sizes  $\Delta x \times \Delta y \times \Delta z = 7.8 \text{ m} \times 7.8 \text{ m} \times 5.25 \text{ m}$ . Again, precursor simulations were performed using periodic lateral conditions (north to south, west to east) with a constant geostrophic wind speed of  $15 \text{ m s}^{-1}$  coming from the southwest ( $225^\circ$ ). The precursor simulations were run for 14400 seconds to develop a fully turbulent, neutrally stratified boundary layer. The values of wind speed and temperature at the south and west boundaries were saved from 7200 s to 14400 s and used as the inlet boundary values to start the wind farm simulations with the 48 wind turbines; top and bottom boundary conditions remained the same as the precursor. The numerical discretization method and the algorithms to solve the system of governing equations are kept the same as in the single- and two-turbine cases (Section 1.3.1). Time-averaged horizontal velocity normalized by hub height wind speed is shown in Fig. 1.17b, where the wakes of the 48 turbines are clearly visible. As far as we know, this is the largest domain and the finest-resolution simulation of a wind farm conducted to date using a compressible framework.

To validate the compressible simulation results, we extracted a subset of the observed power data at each turbine for wind directions between  $215^\circ$  to  $235^\circ$  (using the yaw angle as a proxy for wind direction, as in (Ghaisas et al., 2017)) and with wind speeds between  $11 \text{ m s}^{-1}$  and  $12 \text{ m s}^{-1}$  (corresponding to a geostrophic wind speed of  $\sim 15 \text{ m s}^{-1}$ ), for a total of approximately three months of data. Relative power was computed next as the power of each wind turbine normalized by the power of the

corresponding front turbine of each column and the average was calculated over the three months of interest. Quality checks were performed to ensure that cases with turbine shut-downs for maintenance, or with pitch controls not reproducible in the simulations, or with excessive yaw biases would not be retained. After cleaning the data from all such scenarios, observed relative power for selected columns (E-H) was obtained and compared against the simulated relative power.

In general, the compressible simulation results are in great agreement with the observations 1.18, as the simulated relative power is always within one standard deviation of the observed and often the match is very good. For example, the drop in relative power between the first and second turbine in each column was correctly reproduced, especially in Column H, and so was the flattening of the curves after the second turbine. Note that, in Column E, the third turbine (34) shows a recovery of the relative power because there is a “hole” in the middle of the farm with no turbines (Fig. 1.17a), a feature well reproduced by the simulation. The root mean square error for the four columns is 0.053, 0.038, 0.037 and 0.01, respectively, thus we conclude that the compressible framework proposed here is successful and should be used for future simulations of wind turbine/flow interactions.

### 1.3.5 Conclusions and future work

The booming development of wind energy in the past decade, with turbines becoming increasingly taller and with longer blades, thus larger diameters and rotor areas, brings new challenges to numerical modeling of wind turbines/wind farms and power prediction. For example, the tip Mach number of large wind turbines operating in normal conditions can easily reach  $\sim 0.2-0.3$ , which is usually treated as the upper threshold of incompressible flow. Compressibility effects may arise and alter the flow field as well as the turbine performance. Here, an assessment of such compressibility effects is performed for the first time from two points of view, aerodynamic properties of the turbine blades and variable-density effects.

The Prandtl-Glauert rules are applied to calculate the compressibility corrections to the lift and drag coefficients of the blade airfoils for various combinations of incoming wind speeds and wind turbine rotation speeds. The power coefficient in incompressible flow (no corrections) only depends on TSR and does not change with different incoming wind speeds. However, when compressibility effects are taken into account only to correct the aerodynamic coefficients, the performance of the wind turbine is degraded, but negligibly for low wind speeds and low TSRs. The degradation starts becoming significant when the incoming wind speeds are larger than  $\sim 15 \text{ m s}^{-1}$  and TSR is larger than  $\sim 12$ , both of which are high and rarely occur in real wind farm applications. Therefore, our first conclusion is that compressibility corrections to the aerodynamic coefficients of wind turbine blades ( $C_d$  and  $C_l$ ) are not necessary for simulations of wind farms under normal operating conditions.

Variable-density effects are assessed by performing simulations using both the compressible and the incompressible frameworks and computing their differences. Consistent with our previous conclusion, the aerodynamic coefficients of lift and drag are kept the same in both Comp and Incomp simulations in order to isolate the variable-density effects. Differences between the Comp and Incomp frameworks start to show up when wind turbines are present in the ABL. For a single turbine in the ABL, compressibility effects are not negligible already for Mach number of  $\sim 0.1$  and, although they originate near the tips, they are not limited to the turbine tip region, but are found also in the wake. As the wake propagates, the wind speed and TKE differences between Comp and Incomp also propagate, which leads to lower TKE (up to 15%) and a slightly weaker wind speed deficit in the compressible wake. The exact distribution of the wind speed and TKE differences between Comp and Incomp simulations, in terms of magnitude and horizontal extent, depends strongly on the tip Mach number, thus on TSR. A higher TSR leads to larger compressibility effects and a more confined affected area, while with a lower TSR, the compressibility effects are smaller in magnitude but the affected area extends farther.

In terms of power output, TSR again was the most important factor. For low

TSR, smaller than the optimum value of  $\sim 8$ , power losses due to variable-density effects are very small and so are the effects on the aerodynamic coefficients; thus, for a turbine operating at low TSR, compressibility effects can be safely neglected. When the operating TSR is around the optimum value, the correction in the aerodynamic coefficients still does not affect the power production significantly while power losses due to the variable-density effects start to grow and can no longer be neglected; thus, for a wind turbine operating around the optimum TSR, we expect power losses of about 5%-8% due to compressibility. When the operating TSR reaches a high value ( $>12$ ), the power losses due to variable-density effects and the corrections of the aerodynamic coefficients are both large, thus numerical modeling of intensively operating wind turbines using the incompressible framework might cause large errors; however, wind turbines rarely keep operating in such severe conditions.

The interactions between turbine wakes are then studied via simulations of two aligned turbines. The general behaviour of the first turbine in the two-turbine case is the same as in the single-turbine case. However, after the second turbine, the effects of compressibility on the overlapping wakes behave differently. Looking at wind speed first, the difference between Comp and Incomp becomes less noticeable than in the single-turbine case, thus the power output of the second turbine is approximately the same with the two frameworks. This suggests that the power losses due to compressibility might be limited to the front row of a wind farm, even with multiple rows. However, when considering TKE, compressibility effects appear to be enhanced downwind of the second turbine, with increasingly lower TKE in Comp than Incomp. This suggests that the air flow in a large wind farm with multiple rows of turbines may be significantly less turbulent than previously thought, due to compressibility effects.

The most important implications of these findings are related to wind energy generation and are relevant in many real-world applications. First, since the front row of a wind farm always generates the most power, using the Incomp framework, which is the common practice today, may introduce overestimates of the total wind farm

power. Second, since the power generated by the front turbines is used to calculate relative power, which is the power generated by each turbine divided by that of the front turbine, the relative performance of the inner turbines may be better than previously estimated with the Incomp approach. Third, understanding turbulent wakes, reducing wake losses, and optimizing wind turbine layout including optimization of the turbine hub heights are becoming urgent and important issues in the wind industry ([Archer et al., 2013](#); [Vasel-Be-Hagh and Archer, 2017](#)). This study finds that compressibility effects should not be neglected for such applications because predicting the wake development correctly with the Comp framework could lead to more efficient layout designs, which could lead to benefits of the order of millions of dollars over the lifetime of a wind project.

Since this work is the first to assess compressibility effects in wind farm simulations, more research is obviously recommended. An accurate compressible simulation would require the use of both the corrected aerodynamic coefficients and the variable-density compressible framework together, as opposed to separately as was done here. Without the need for consistency between Incomp and Comp that was crucial in this paper to compute meaningful differences, more advanced numerical methods can be chosen for the compressible simulations, such as a more sophisticated turbulence closure or large eddy simulation with a dynamic turbulence model. Third, it is recommended that the combined effects of buoyancy and compressibility via simulations of the stable and unstable atmospheric boundary layer in the presence of turbines be assessed using the compressible framework, since this paper has focused on neutral stability with effectively no buoyancy. Lastly, aeroelastic coupling between the compressible air flow and the turbine blade structure, which requires algorithms linking structural dynamics and aerodynamics ([Sørensen, 2011](#)), is needed to assess the effects of compressibility on the flexibility of the blades.

In conclusion, compressibility effects associated with large horizontal-axis wind turbines cannot be neglected because ignoring them would cause an overly optimistic prediction of a wind farm power production. It is therefore recommended that future

numerical studies of the flow around wind turbines be based on a compressible framework, as opposed to the commonly-used incompressible and Boussinesq framework.

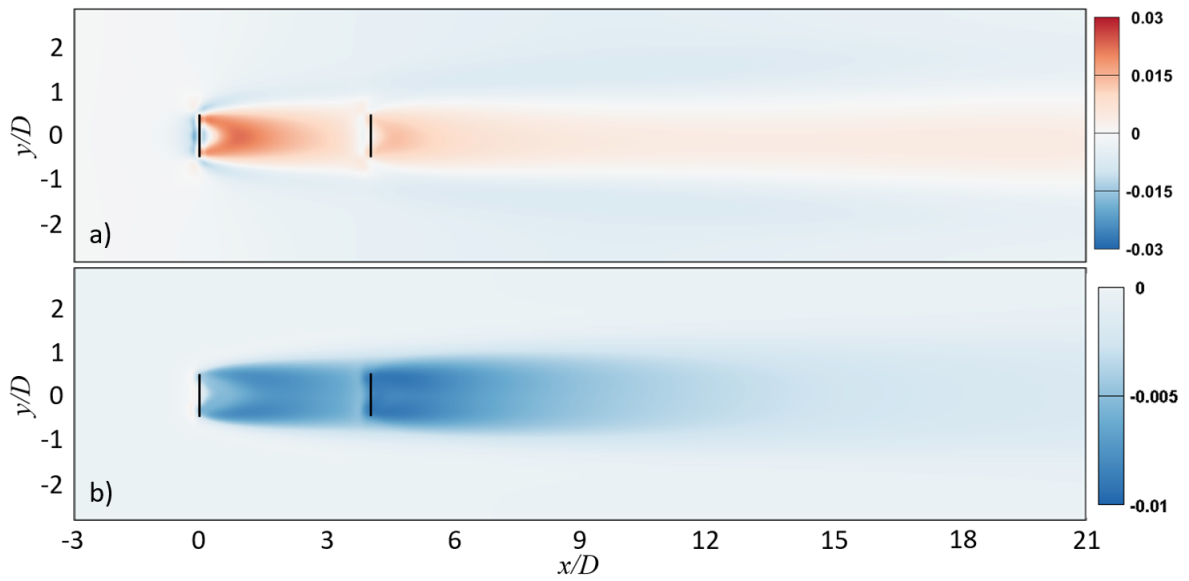


**Figure 1.15:** Case 5: horizontal cross-sections of: a) Comp - Incomp wind speed difference and b) Comp - Incomp TKE difference at hub height, normalized by  $U_{hub}$  and  $U_{hub}^2$  respectively, for the two-turbine case in Table 1.3.

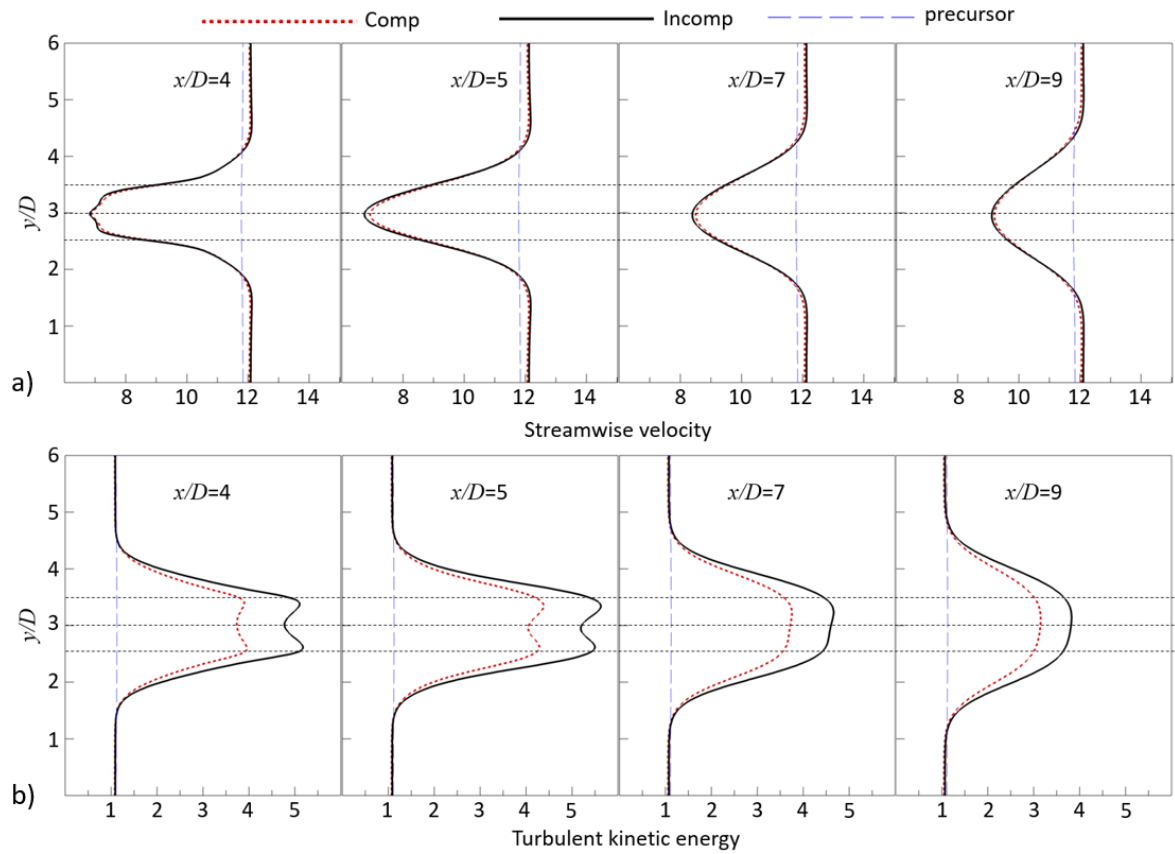


**Figure 1.16:** Case 5: horizontal profiles of: a) wind speed ( $\text{m s}^{-1}$ ) and b) TKE ( $\text{m}^2 \text{s}^{-2}$ ) at hub height for the two turbine case, starting at the position of the second turbine ( $4D$  after the first turbine).

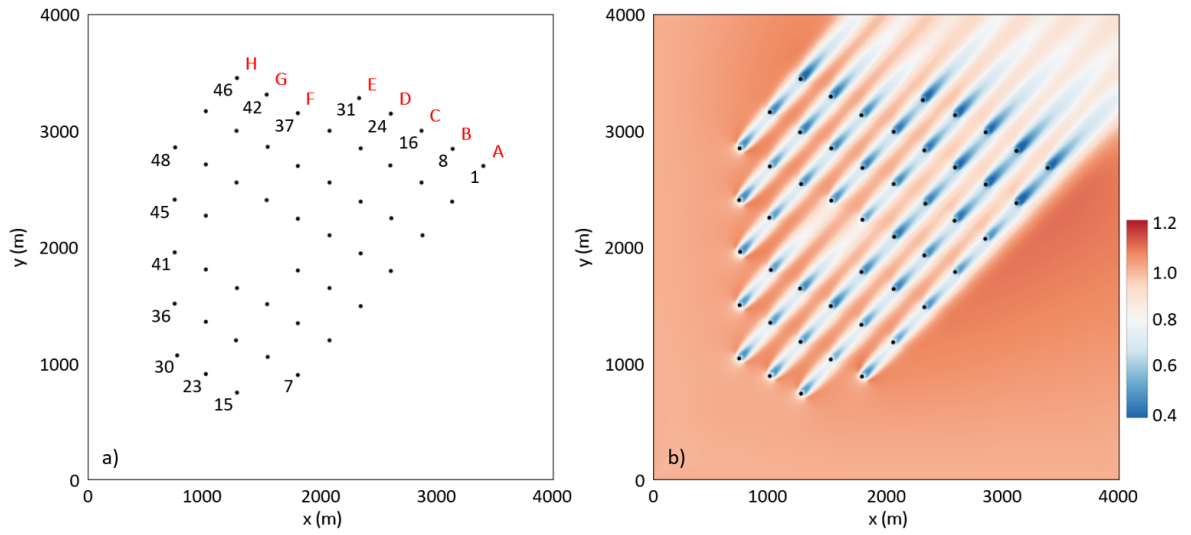


**Figure 1.17:** a) Computational domain and location of the 48 turbines in the Lillgrund wind farm; and b) time-averaged horizontal velocity normalized by hub height wind speed with wind coming from  $225^\circ$  using the compressible framework.

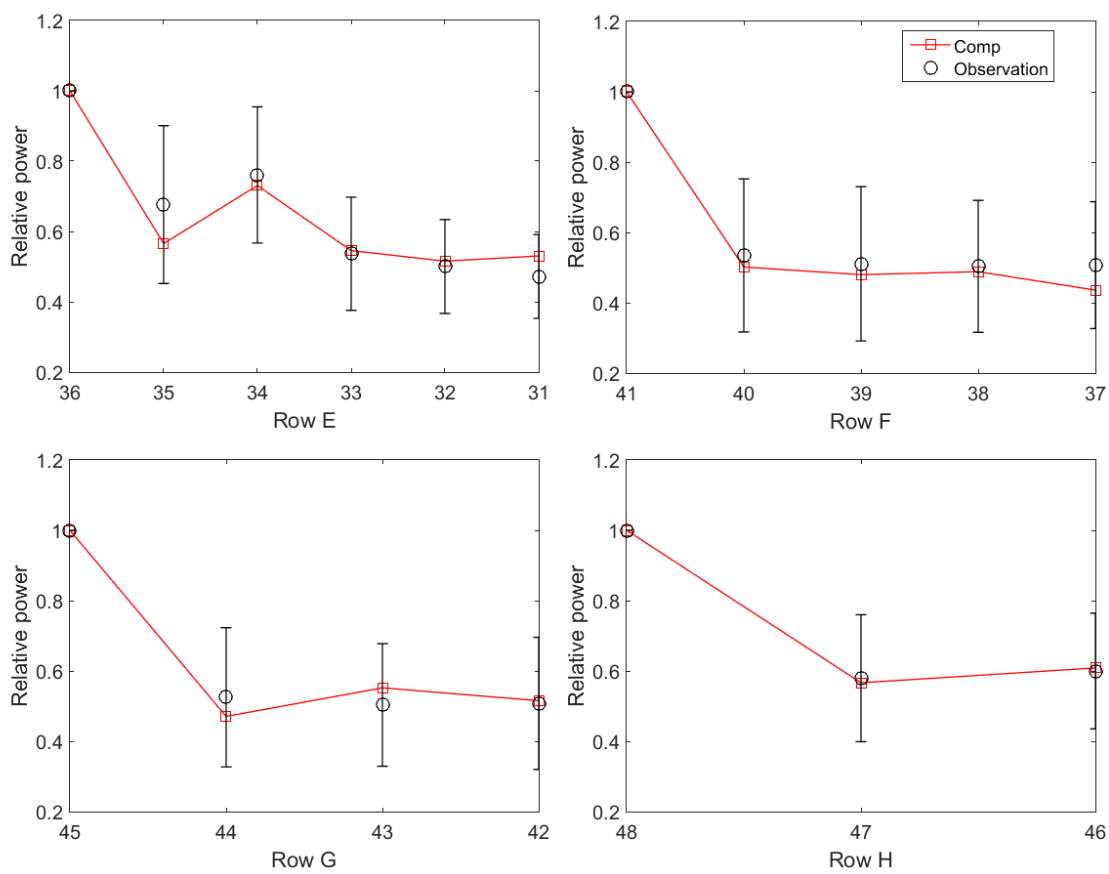


**Figure 1.18:** Time-averaged relative power simulated with the compressible framework versus observed for columns E-H at the Lillgrund wind farm.

## Chapter 2

# A GENERAL METHOD TO ESTIMATE WIND FARM POWER USING NEURAL NETWORKS

### 2.1 Introduction

Wind energy has grown to be one of the largest sources of renewable energy, with an installed capacity expected to exceed 800 GW by the end of 2021 (GWEC, 2016). An increasing fraction of the generating capacity is being switched from fossil fuels to wind power, which will help reduce the emissions of greenhouse gases. However, the actual output of a large wind farm is not simply the sum of the power generated by the individual turbines at the upstream (or undisturbed) wind speed, as interactions between turbine wakes play an essential role and can significantly reduce the total power output. As a result, correctly estimating power output and wake losses for both existing and future large wind farms is critical.

Physics-based (or physical) methods have been widely studied and used for power estimation of large wind farms, including: mesoscale numerical weather prediction models with wind turbines parameterized as elevated kinetic energy sinks (Jacobson and Archer, 2012; Marvel et al., 2012; Fitch et al., 2013; Jacobson et al., 2014); large-eddy simulations (Wu and Porté-Agel, 2011; Churchfield et al., 2012a; Archer et al., 2013; Xie and Archer, 2015) and Reynolds-averaged Navier-Stokes simulations (Schlunz and Willden, 2015; Yan and Archer, 2018) with wind turbines represented by actuator lines (Sørensen and Shen, 2002; Troldborg et al., 2010; Lu and Porté-Agel, 2011) or actuator disks (Sørensen and Kock, 1995; Masson et al., 2001; Alinot and Masson, 2002); and kinetic models based on momentum theory (Jensen, 1983; Larsen, 1988; Ainslie, 1988; Frandsen et al., 2006). The main drawback of physical models

is that they are computationally expensive, thus cannot be applied efficiently to predict the power output of a large wind farm with different combinations of operational parameters, such as wind speed, wind direction, and layout.

Instead of complex and computationally-demanding physical models, machine learning (ML) methods have gained popularity in estimating wind farm power output and wake losses. By building linear or non-linear relationship between the input and output data, ML methods can learn the hidden information patterns automatically with sufficient training (Lei et al., 2009). Among the ML methods, Artificial Neural Networks (ANN) have been increasingly used due to their robustness, noise insensitivity, and ability to perform complex regressions for multi-variable applications (Hornik et al., 1989; Schmidhuber, 2015). In Carolin Mabel and Fernandez (2008), wind speed, relative humidity, and generation hours were used as inputs to train the ANN; the predicted wind farm power output compared well with observations. In Blonbou (2011), wind speed and wind power at the previous time step were used to train the ANN along with adaptive Bayesian learning and Gaussian process approximation; the resulting wind power prediction performed better than the reference persistence model. In Kelouwani and Agbossou (2004), average wind speed, wind speed standard deviation, and past power output were used as inputs to train the ANN; the power prediction outperformed a more complex stochastic model. Long-range time series prediction of wind speed and power for a wind park using a Recurrent Neural Network (RNN) were performed in Barbounis et al. (2006). Short- and long-range power predictions using RNN with a Kalman-filter based back-propagation algorithm were performed in Li (2003) and better results in long-term prediction were obtained.

Despite its many advantages in estimating wind farm power, the successful training of a Neural Network (NN) heavily relies on the quantity and quality of the collected data. Furthermore, all previously-trained NNs are wind-farm specific, which means that, once a NN is fully trained, it can only be used for the wind farm where the data were collected.

In this paper, we propose a new way to train a NN and, for the first time, we

use the NN trained on a wind farm to estimate the power output of another wind farm.

## 2.2 Data and methods

### 2.2.1 Pre-processing of the Lillgrund wind farm data

The data used in this study were collected at the Lillgrund offshore wind farm, located off the coast of Sweden in the Baltic Sea. Lillgrund contains 48 Siemens SWT-2.3MW wind turbines, with turbine spacing of  $4.3D$  (where  $D$  is the rotor diameter, 63 m) along the southwest and  $3.2D$  across it (Figure 2.1). Such a tight spacing makes Lillgrund an ideal site for the current study because wind turbine wakes play an essential role in the total wind farm power output. The operation information, including wind speed, wind direction, and turbine power output, was collected by the SCADA system installed at every turbine. The data used for the current research cover a period of approximately three years at a temporal resolution of 1 minute and were quality-checked and cleaned using the method described in Ghaisas et al. (2017).

The variable that most significantly influences the wind farm power output is wind speed (Miller et al., 1997). Wind speed from a nearby meteorological tower, located about 200 m to the southwest of the Lillgrund wind farm, could be treated as the undisturbed incoming wind speed. However, for a wide range of wind directions, the meteorological tower is affected by the wake of the entire wind farm, thus the wind speed readings cannot be used. Wind speeds from the sensors on the individual turbines cannot be directly used either, as the inner wind turbines are always affected by wakes. As such, we compute the maximum wind speed from all the turbines at each time step and treat it as the incoming wind speed for the whole wind farm ( $U$ ).

The second variable that significantly affects the whole wind farm power is wind direction  $\theta$  (Wu and Porté-Agel, 2013). The median of all 48 yaw angles is computed at each time step and treated as a proxy representative of the incoming wind direction. Since the incoming wind speed and wind direction will both be used as inputs to the NN, it is important that they are normalized, otherwise the wind direction, which scales to a maximum value of 360, will wash out the effects of wind speed, which never

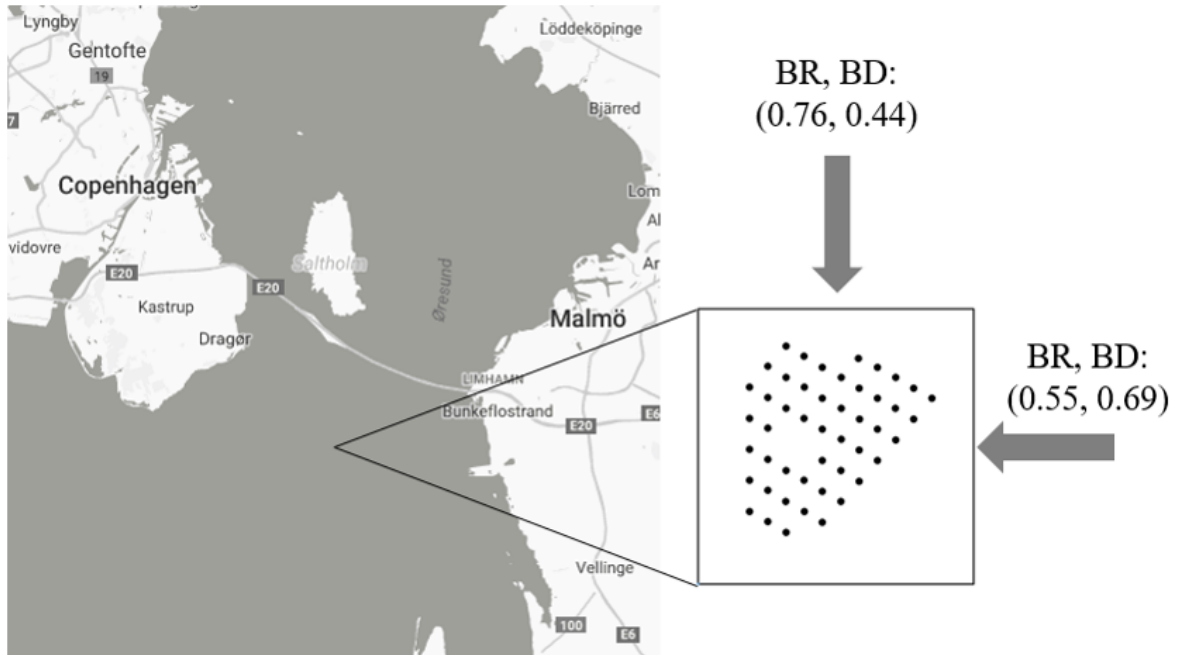


**Figure 2.1:** Location and layout of the Lillgrund offshore wind farm located between Denmark and Sweden, with geometric properties (BR, BD) for northerly and easterly wind directions.

exceeds  $30 \text{ m s}^{-1}$ . Note that, for the actual NN calculations, we convert wind speed and direction to the west-to-east and south-to-north components of the wind vector  $(u, v)$ , after conversion from the meteorological to the Cartesian convention.

In addition to the fact that different wind directions induce different wake losses for a certain wind farm layout, even for the same wind direction, the wake losses will differ for two different wind farm layouts. For each wind direction, we therefore calculate two parameters, to be treated as two additional inputs in our NN described later: the Blockage Ratio (BR) and the Blockage Distance (BD), introduced by Ghaisas and Archer (2016).  $BR_i$  is the fraction of the swept area of turbine  $i$  that is blocked by the swept area of any upstream turbine.  $BD_i$  represents the weighted-average distance to the upstream blocking turbines.  $BR_i$  and  $BD_i$ , both varying over  $[0,1]$ , are defined as follows:

$$BR_i = \frac{1}{A} \int_{(x,y) \in A} \chi dx dy, \quad (2.1)$$

$$BD_i = \frac{1}{A} \int_{(x,y) \in A} [\chi L + (1 - \chi) L_\infty] dx dy, \quad (2.2)$$

where  $A$  is the swept area of the rotor disk and  $(x, y)$  are grid points on the rotor disk. The function  $\chi$  equals 1 if the grid point is blocked by any upwind turbine, otherwise 0.  $L$  is the distance between the grid point and any upwind blocking turbine and  $L_\infty$  is used for grid points not blocked by any upwind turbines and is set to  $20D$ , since wind turbine wakes usually recover within  $20D$  (Wu and Porté-Agel, 2011; Xie and Archer, 2015).

For every wind direction in the data set,  $BR_i$  and  $BD_i$  are first calculated for each turbine  $i$  and then averaged over the  $N=48$  turbines to get a single BR and BD for the whole wind farm:

$$BR = \frac{\sum_i^N BR_i}{N}, \quad BD = \frac{\sum_i^N BD_i}{N}. \quad (2.3)$$

The last relevant parameter, which will also be the output of the final layer of the NN, is the relative power for the whole wind farm:

$$P_r = \frac{\sum_i^N P_i}{NP_{front}} = \frac{P}{NP_{front}}, \quad (2.4)$$

where  $P_i$  is the observed (or NN-simulated) power of turbine  $i$ ,  $P$  is the total power output of the entire wind farm, and  $P_{front}$  is the unblocked front-row turbine power (assumed to be the highest power generated by any turbine at each time step).

### 2.2.2 Architecture and training of the neural network

In this work, a deep neural network is used for the power estimation system (“deep” omitted hereafter). The NN is constructed with one input layer, two hidden layers with 50 and 40 neurons, and one output layer (Figure 2.2). Inspired by the biological brain, each layer of the NN consists of many nodes called artificial neurons, which can communicate with nodes in further layers through connecting synapses. The synapses between each layer are associated with a weight, which controls the strength of signals passing through each node.

The algorithm for training the NN contains two main steps: forward and backward propagation.

In the forward propagation, the input signals (e.g., wind speed and wind direction in the simplest case) are fed to the NN to obtain, by parallel calculations using a weight matrix  $w$  and an activation function  $\sigma$ , the NN output  $\hat{P}_r$ . The mathematical expression of the signal flow  $x_j^l$  through a layer  $l$  is:

$$x_j^l = \sigma \left( \sum_i w_{ji}^l x_i^{l-1} + b_j^l \right) = \sigma(z), \quad (2.5)$$

where  $x$  is either  $U$  and  $\theta$  in the traditional NN or  $U$ ,  $\theta$ , and (BR,BD) in the GM-trained NN described later in Sections 2.3.1 and 2.3.2 (Figure 2.3 and 2.4),  $w_{ji}$  is the weight matrix connecting the  $i^{th}$  node output in the previous layer  $l-1$  to the  $j^{th}$  node in the current layer  $l$  and  $b_j^l$  is the bias on the  $j^{th}$  node in the current layer  $l$ . The expression inside the parenthesis ( $z$ ) is the input signal for the current layer, then an

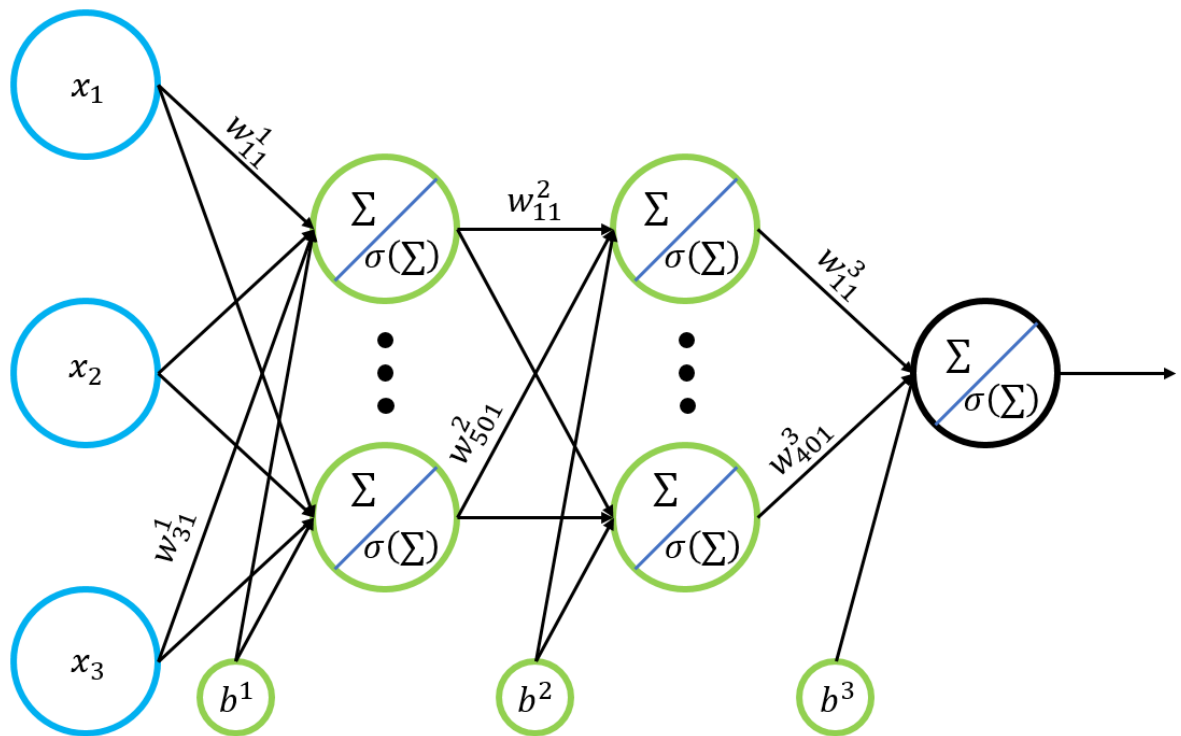


**Figure 2.2:** Architecture of the neural network, with two hidden layers (in green) containing 50 and 40 neurons.

activation function  $\sigma(z)$  is applied to it to get the output signal for the current layer. We use the hyperbolic tangent function for  $\sigma$  because of its non-linearity:

$$\sigma(z) = \frac{e^z - e^{-z}}{e^z + e^{-z}}. \quad (2.6)$$

In the backward propagation, the error signals are computed for the output layer:

$$e = \hat{P}_r - P_r \quad (2.7)$$

and then used to correct and refine the weights in each layer using a loss function  $L$ , in this case the mean square error:

$$L = \frac{1}{n} \sum^n e^2, \quad (2.8)$$

where  $n$  is the number of sample data sets. The weight and bias of each layer are traditionally updated using the gradient descent method. The derivatives of the loss function in terms of weight and bias are calculated recursively back through each layer using the chain rule, then the weight and bias of each layer are adjusted based on the derivatives in order to reach the minimum loss by updating the weights matrix  $w$  as follows:

$$w = w - \eta \frac{\partial L(w)}{\partial w}, \quad (2.9)$$

where  $\eta$  is the learning rate. The original gradient descent method can be very slow when the local gradient is small, which is critical for training large amounts of data. It also cannot deal with the situation when the loss curve is much steeper in one dimension than in the other dimensions (Sutton, 1986). Inspired by the physical concept of momentum, Polyak (1964) proposed the momentum optimization method:

$$m = \beta m + \eta \frac{\partial L(w)}{\partial w}, \quad (2.10)$$

$$w = w - m, \quad (2.11)$$

where  $m$  is the momentum matrix and  $\beta$  is a constant ranging from 0 to 1. The momentum optimization method runs faster than the regular gradient descent. Variants

of other gradient descent method have been developed, such as AdaGrad (Duchi et al., 2011), AdaDelta (Zeiler, 2012) and RMSProp (Tieleman and Hinton, 2012). In the current work, we adopt the Adaptive Moment Estimation (Adam) method (Kingma and Ba, 2014), which keeps the exponentially decaying average of past gradients  $m$  (first moment), similar to momentum method. It also keeps track of the exponentially decaying average of past squared gradients  $v$  (second moment), similar to RMSProp. The Adam algorithm consists of five main steps:

$$m = \beta_1 m + (1 - \beta_1) \frac{\partial L(w)}{\partial w}, \quad (2.12)$$

$$v = \beta_2 v + (1 - \beta_2) \frac{\partial L(w)}{\partial w} \circ \frac{\partial L(w)}{\partial w}, \quad (2.13)$$

$$m = \frac{m}{1 - \beta_1^t}, \quad (2.14)$$

$$v = \frac{v}{1 - \beta_2^t}, \quad (2.15)$$

$$w = w - \frac{\eta}{\sqrt{v} + \epsilon} m, \quad (2.16)$$

where  $\beta_1$  and  $\beta_2$  are the exponential decay rates for the first and second moment,  $t$  is the iteration step, “ $\circ$ ” denotes the element-wise multiplication, and  $\epsilon$  is the smoothing constant. Adam is an adaptive learning method, thus require less tuning, it is computationally efficient, and it outperforms other stochastic optimization methods (Kingma and Ba, 2014).

In machine learning, the procedure of training through the whole data set is called an epoch. There are three ways of training through one epoch: batch, stochastic, and mini-batch. The batch training treats the whole data set as a whole batch and the weight matrices are updated only once per epoch using a gradient descent-like optimizer. Batch training usually has computing memory issues for large data sets. Since only one update is done per epoch, in order to reach the minimum loss, sometimes hundreds of epochs are required for large data sets. The stochastic training, on the other hand, performs one update on the weight matrices per data sample in the data set, thus for an epoch that contains a million data samples, the weight matrices would need to be updated a million times. Stochastic training is faster than batch training

and does not have memory issues. However, since the optimization is performed on each data sample, stochastic training is very sensitive to outliers and requires high-quality data, otherwise it will have unstable convergence issues. In this study, we use the third training procedure: mini-batch training. For one epoch, the whole data set is divided into many mini-batches. In our Lillgrund wind farm case, a mini-batch consists of 50 data samples. Mini-batch training combines the advantages of batch training and stochastic training, because it allows multiple updates in one epoch while it decreases the sensitivity to outliers, thus can obtain a fast and stable convergence.

We use k-fold cross validation (Bishop, 2006) to train and evaluate our deep NN for the Lillgrund wind farm. In brief, the whole data set is divided into k randomly-assigned subsets (k=3 in this study). As one of the k subsets is reserved for testing, the neural network is effectively trained on k-1 subsets and its accuracy is then measured against the test set. The whole process is repeated several times using different subsets as the test set, then the final hyper parameters of the NN are chosen based on the best average performance.

### 2.3 Results

In the traditional approach, hereafter referred to as traditional NN (Figure 2.3), the two inputs are wind speed and direction ( $U$  and  $\theta$ ) and the output is either total or relative power ( $P$  or  $P_r$ ). Once the traditional NN is trained, it can be used to estimate future power output (total or relative) at Lillgrund with a high degree of accuracy. In the new approach proposed in Section 2.3.2, hereafter referred to as GM-trained NN because it is based on the Geometric Model (GM) introduced by Ghaisas and Archer (2016), an extra step is needed to calculate BR and BD for each wind direction (Figure 2.4). The accuracy of the GM-trained NN is slightly lower than that of the traditional NN at Lillgrund, but the huge advantage is that the trained GM-trained NN can be used to predict total or relative power at any wind farm, not just at Lillgrund.

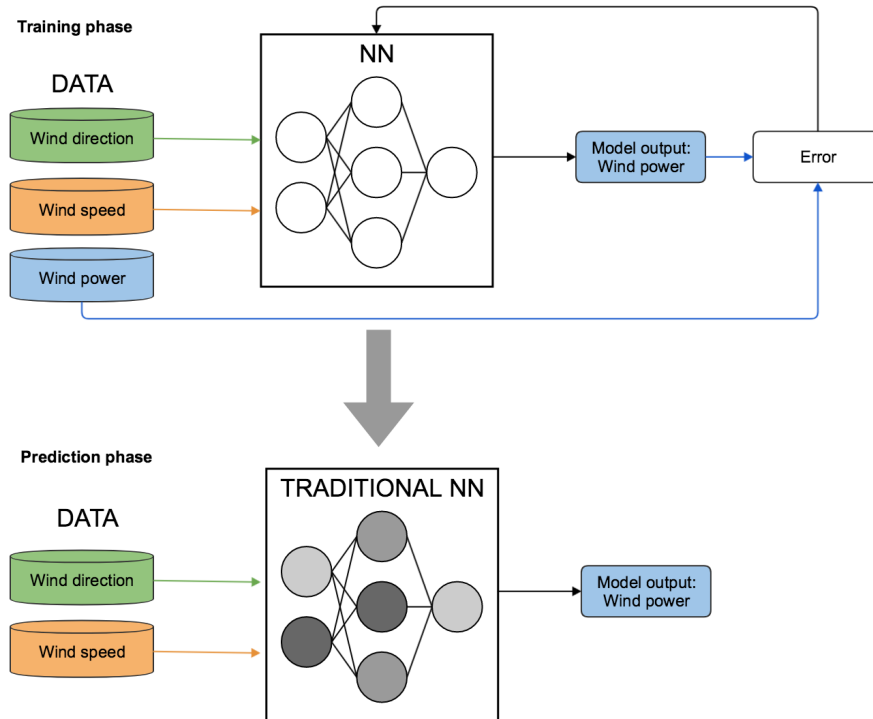


**Figure 2.3:** Flowchart of the traditional deep neural network (NN) developed with the Lillgrund wind farm data. In the traditional NN, the inputs (wind speed and direction) and output (power) at the Lillgrund wind farm are used to train the NN, which ultimately can be used to estimate future power at Lillgrund with high accuracy. The traditional NN cannot be used at another wind farm.

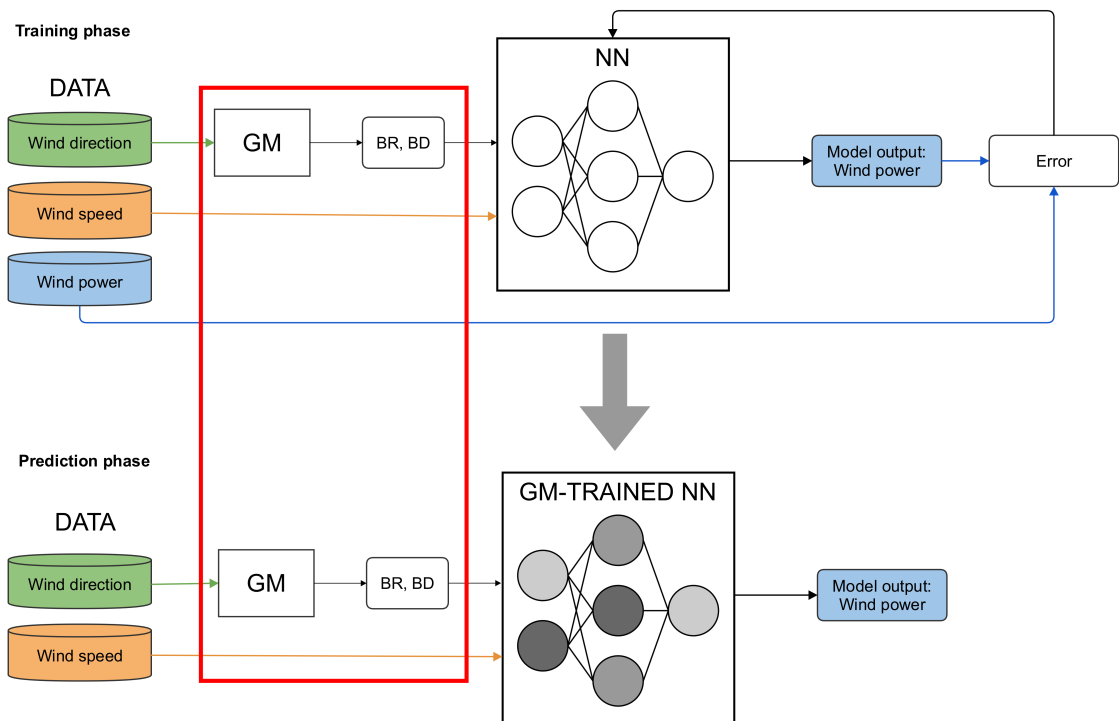


**Figure 2.4:** Flowchart of the GM-trained NN developed with the Lillgrund wind farm data. In the GM-trained NN (include the red box), an additional step is needed to calculate BR and BD with the Geometric Model (GM), but then the trained NN can be used at any wind farm, not just at Lillgrund.

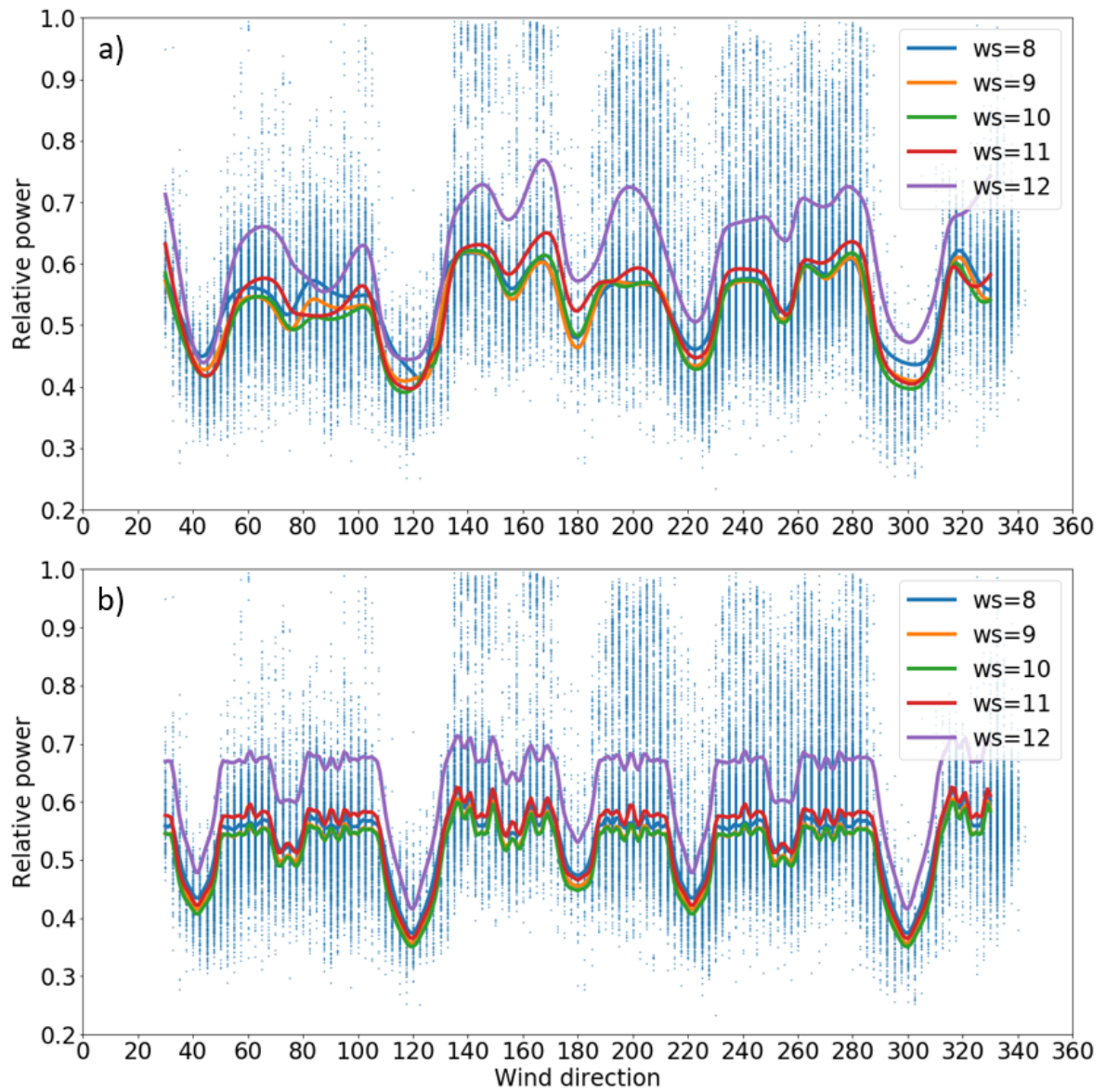
### 2.3.1 Traditional NN to estimate power at Lillgrund only

Figure 2.5a shows the observed relative power for all wind speeds and directions at Lillgrund for all turbines (a total of 83,933 data points). For each wind direction, there is a large scatter in the observed relative power because all the turbines are included, some of which are front-row, thus producing relative power equal to one, while the others produce less. The four wind directions that are associated with the largest wake losses (and therefore with the minima in relative power) are  $42^\circ$ ,  $120^\circ$ ,  $222^\circ$  and  $300^\circ$ , which are the four directions of alignment of the turbines in the Lillgrund layout. The pattern of relative power is not repeated exactly every  $180^\circ$  because meteorological and geographic factors, such as wind speed frequency distribution, atmospheric stability, turbulence intensity, or local terrain heterogeneity, may not be the same for pairs of opposite wind directions.

The observed patterns in relative power are reproduced very well by the traditional NN (Figure 2.5a). For a wide range of wind speeds ( $8\text{--}11\text{ m s}^{-1}$ ), relative power maintains almost exactly the same patterns, which is consistent with previous findings (Creech et al., 2015). However, as the wind speed increases and reaches the rated wind speed ( $12\text{ m s}^{-1}$ ), relative power increases (or wake losses decrease), because at high wind speeds the blade pitch control system forces the turbines to produce no more than the rated power, thus more kinetic energy is left in the flow for the blocked inner wind turbines and therefore the whole wind farm relative power is higher.

The performance of the traditional NN is excellent, as indicated by four commonly-used error metrics (Foley et al., 2012): the mean error (bias= $-0.0052$ ), the mean absolute error (MAE= $0.020$ ), the standard deviation of the MAE ( $\sigma_{MAE}=0.027$ ) and the root mean squared error (RMSE= $0.028$ ).

Another useful application of the traditional NN is the calculation of a two-dimensional power curve for the entire wind farm. The power curve is a manufacturer-provided, one-dimensional relationship between the hub-height wind speed and the power output expected from a single turbine. However, in a wind farm with multiple turbines and wake losses, the power curve cannot be used directly because power



**Figure 2.5:** Relative power at Lillgrund from observations (blue dots) and predictions (colored lines) with: a) traditional NN and b) GM-trained NN.

generation is no longer just a function of wind speed, but rather a function of wind speed, direction, and layout. With the estimate of relative power as a function of wind speed and direction at Lillgrund from the traditional NN, it is possible to construct a two-dimensional power curve for the entire wind farm (Figure 2.6). This is the first two-dimensional power curve based on a deep NN published in the literature.

### 2.3.2 GM-trained NN to estimate power at any wind farm

The GM-trained NN requires an additional step, which is the replacement of wind direction with combinations of BR and BD obtained through Eqs. 2.1-2.2. As indicated by the red box in Figure 2.4, each wind direction corresponds to a specific combination of BR and BD.

The GM-trained NN (Figure 2.5b) exhibits more “wiggles” than the traditional NN (Figure 2.5a), due to the relatively high sensitivity of the geometric properties to small changes in wind direction. However, the important patterns of high and low relative power (i.e., low and high wake losses) are well reproduced, including the dependency on wind speed.

The GM-trained NN has a similar but slightly lower performance than the traditional NN (bias=-0.0037, MAE=0.035,  $\sigma_{MAE}$ =0.039, and RMSE=0.041), which is expected, because of two reasons. First, the complex layout of the wind farm is represented using just two easy-to-calculate geometric properties. Second, the geometric properties are intrinsically cyclic by 180° by design, therefore the observed relative power differences at Lillgrund for wind directions that are 180° apart cannot be reproduced by the GM-trained NN (or by any other analytical wake loss model, unless additional inputs are provided to differentiate the pair). However, the small loss in performance at Lillgrund is more than compensated for by the fact that the GM-trained NN is general and therefore can be used at other wind farms.

All available observed combinations of BR and BD for the Lillgrund wind farm for all wind directions at a 5-degree resolution, for all wind speeds, are learned by the GM-trained NN. The actual values for wind speed of 8 m s<sup>-1</sup> are shown in Figure

2.7a. Note that only the upper-right corner includes data in Figure 2.7 because of the dependency of BD on BR in Eq. 2.2. The wind farm relative power is lowest at high BRs and low BDs (directions of alignment), indicated by the dark blue points at the lower right corners. The maximum power is generated at low BRs and high BDs (directions of non-alignment), indicated by the points at upper left corner. For the same BR, the wind farm relative power increases as BD increases, as wind turbine wakes have a longer distance to recover when BD increases.

The powerful feature of the GM-trained NN is that, once we introduce BR and BD instead of wind direction, we are no longer limited to the current wind farm. The GM-trained NN can use the information learned at Lillgrund to predict the power of more combinations of BR and BD, which do not exist at Lillgrund and represent different wind farm layouts. Figures 2.7b-f show the wind farm relative power for all combinations of BRs and BDs at different wind speeds. The general pattern of power is consistent with the previous findings: little to no change for a wide range of speeds, followed by an obvious increase as the wind speed approaches rated wind speed. As BR approaches zero, which means that no wind turbines are blocked, the wind farm has no wake losses and relative power is one. As BD approaches one (corresponding to a distance of 20D or more), which means that every wind turbine is far away from any other, there are also no wake losses for the wind farm and relative power is one. When BR is high but BD is low, which means most turbines are blocked and are very close to their front-row turbines, minimum power production is expected, indicated by the dark blue corner.

### 2.3.3 Transfer learning: Application of the GM-trained NN to the Nørrekær wind farm

After the GM-trained NN has been trained on available combinations of BR and BD from existing data (Figure 2.7a), we can predict wind farm relative power for all other different combinations of BR and BD (Figures 2.7b-f). For the first time, a transfer learning method for power loss estimation for any wind farm layout is

proposed. The predictions for combinations of BR and BD unseen at Lillgrund, i.e., different layouts, are tested on the Nørrekær Enge wind farm. Nørrekær is located onshore in northern Denmark. It consists of 13 equally-spaced and perfectly aligned Siemens 2.3-MW turbines, with two directions of alignment at  $75^\circ$  and  $225^\circ$  (Figure 2.8).

The observation data at Nørrekær, including wind direction, wind speed, and wind farm power are first quality-checked using the same procedure described in Sec. 2.2.1, leaving a total of 181,071 valid observations; then, for each wind direction, the corresponding BR and BD are calculated and used as input for the GM-trained NN. The general pattern of relative power is captured very well (Figure 2.9), with large wake losses around the two directions of alignment and a relatively constant relative power around one for the remaining directions. Similar to previous results, relative power remains approximately the same for intermediate wind speeds and increases when wind speed approaches the rated wind speed. The statistical performance at Nørrekær is comparable to that at Lillgrund, with bias=-0.0069, MAE=0.061,  $\sigma_{MAE}$ =0.064, and RMSE=0.067.

The layout of Nørrekær is a straight line, thus for the directions of non-alignment BR is zero and BDs is one, thus the relative power prediction from the GM-trained NN is one (i.e., no wake losses). However, the observed power for the directions of non-alignment is not exactly one. Several reasons can cause this: atmospheric stability, non-homogeneous winds, different turbine operation and maintenance, sensor malfunction, etc. None of these features can be captured by the neural network, or any other wake loss model.

## 2.4 Conclusions

We present an innovative technique to predict wind farm power using machine learning, more specifically, a deep NN. The traditional way of training a deep NN for wind farm power has the advantage that it generates a two-dimensional power curve that provides possibly the most accurate prediction of wind farm power given wind

speed and direction. However, it also has a major limitation, which is that the trained NN can only be used for the specific wind farm where the data were collected. A new way to train the deep NN is proposed in this work. By adding a simple geometric calculation step, the trained NN, which we call GM-trained NN, can now be used to perform predictions of power production at any wind farm.

K-fold cross validation is used to compare the performance of the two NNs at the Lillgrund wind farm. Both show very high accuracy, with  $MAE < 5\%$ , although the error of the traditional NN is slightly better than that of the GM-trained NN, which is expected. The ultimate purpose of the new method is to equip the NN with the ability of predicting other wind farms without compromising the accuracy too much. Next the GM-trained NN that was trained with data observed at Lillgrund is used to predict the power of another wind farm, i.e., Nørrekær. The sudden drops near the two directions of alignment are well captured. The observed relative power for the directions of non-alignment are not exactly one, possibly due to atmospheric stability, non-homogeneous wind, etc., which are features not captured by the simple geometric properties used as inputs. Nonetheless, the statistical performance of the GM-trained NN at Nørrekær is still very good, with  $MAE=0.061$ ,  $\sigma_{MAE}=0.064$ , and  $RMSE=0.067$ .

Future work includes: the tuning of the geometric properties to eliminate some of the excessive sensitivity to wind direction; the testing of other geometric properties in addition to blockage ratio and blockage distance, like inverse blockage distance; further validation at other wind farms, offshore and inland, and with different turbine models; an assessment of the sensitivity of the wind speed and direction data and predictions to the bin size; and the use of the GM-trained power curve as a simplified wind farm parameterization to be used in mesoscale or climate model to model the effects of the entire wind farm on the wind flow.

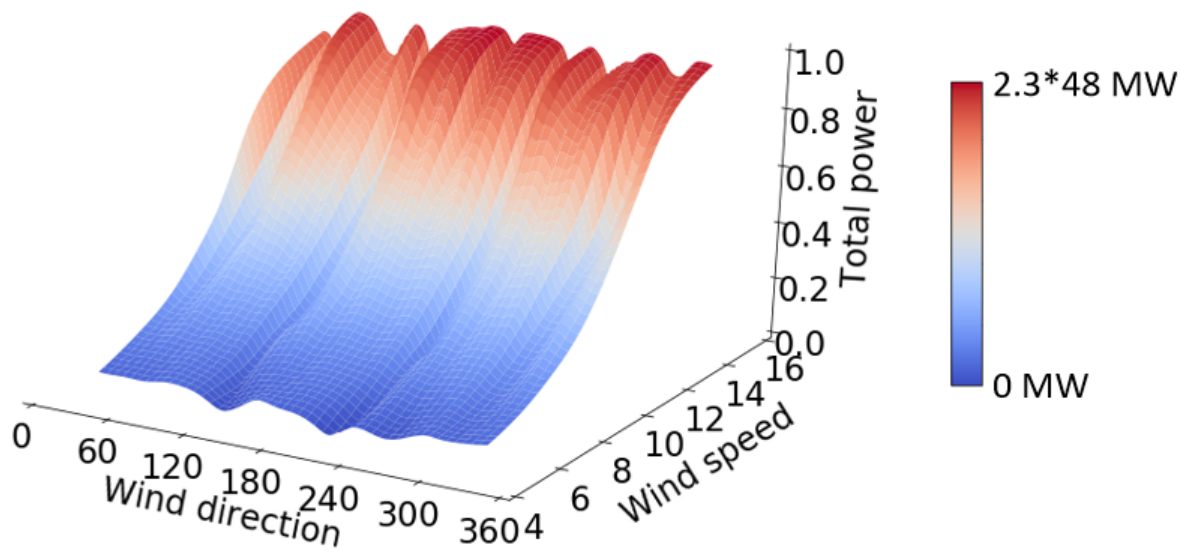


**Figure 2.6:** Two-dimensional wind farm power curve predicted with the traditional NN for Lillgrund.

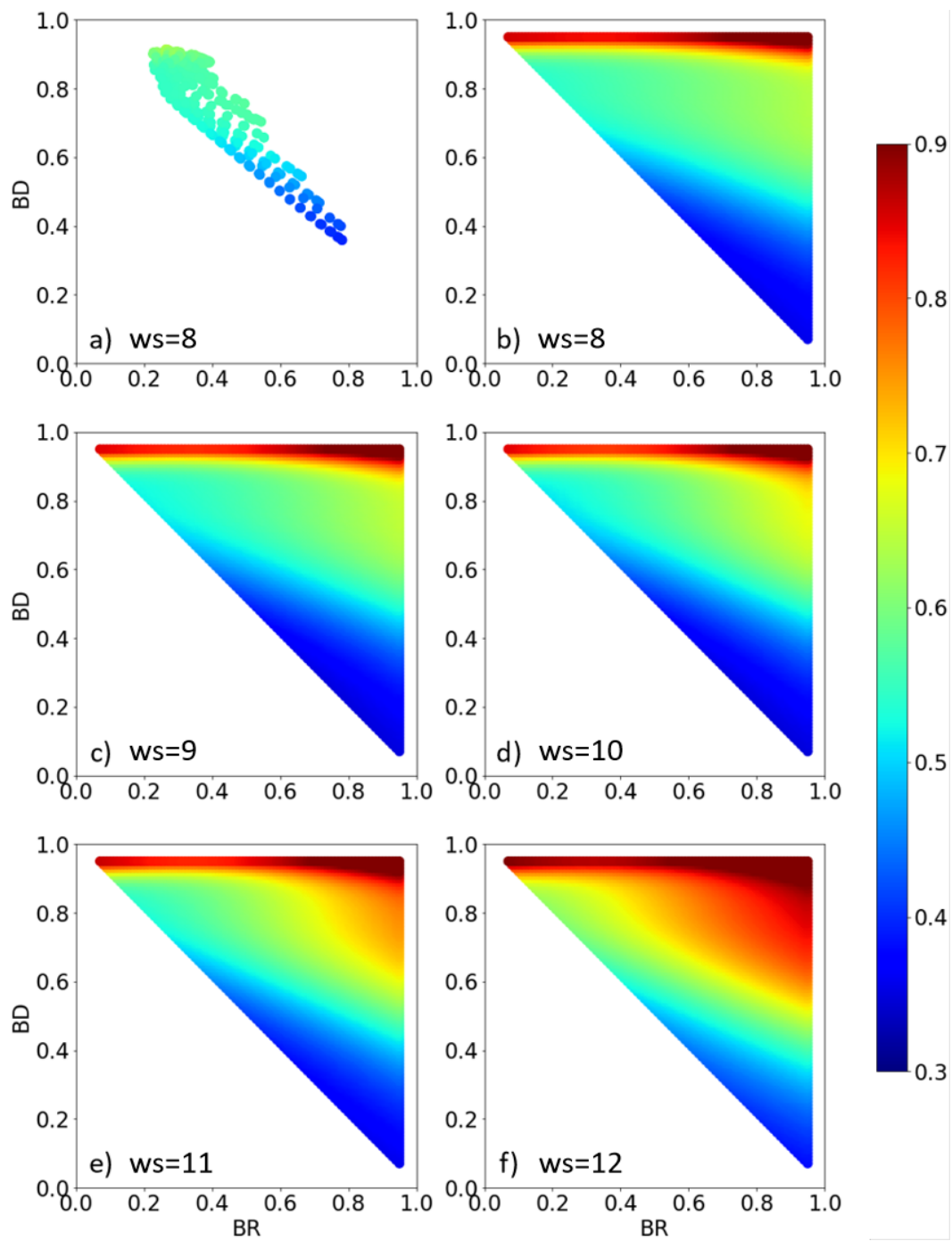


**Figure 2.7:** Relative power as a function of BR and BD: a) observed at Lillgrund at a wind speed of  $8 \text{ m s}^{-1}$ ; b-f) predicted by the GM-trained NN at different wind speeds ( $8\text{-}12 \text{ m s}^{-1}$ ).

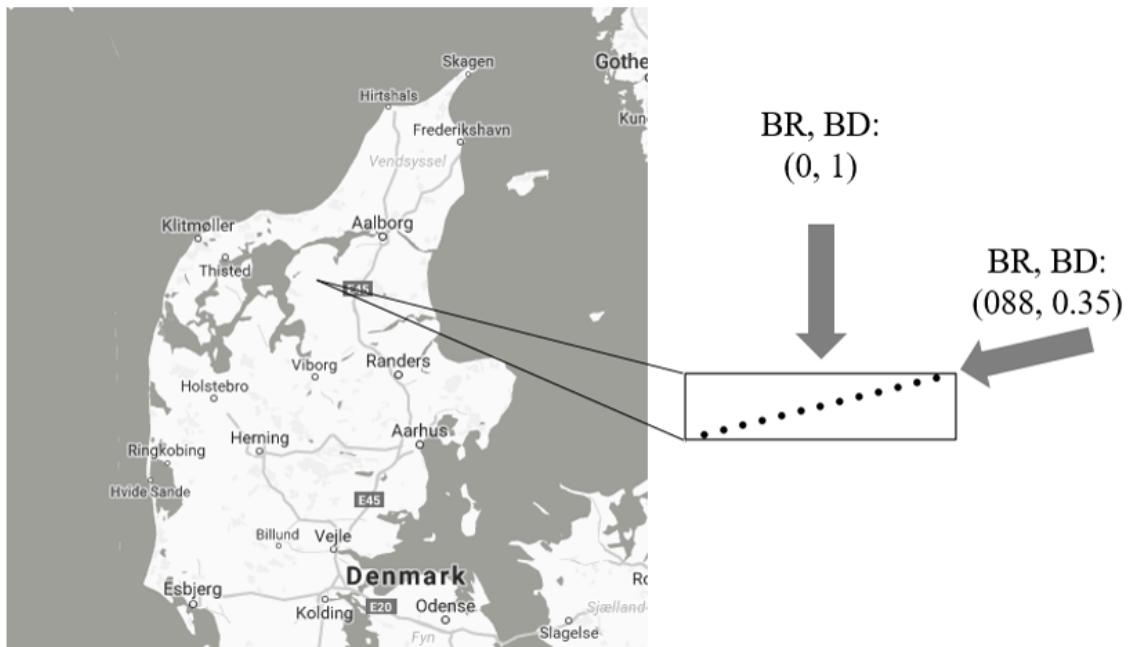


**Figure 2.8:** Location and layout of Nørrekær with geometric properties (BR, BD) at certain wind directions.

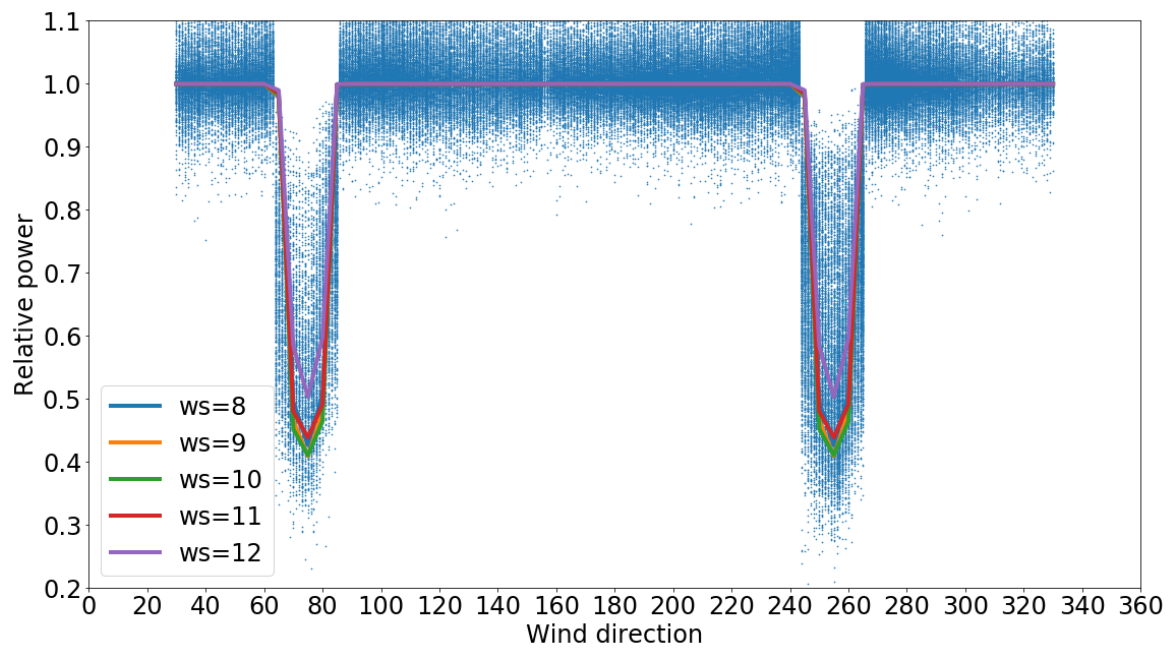


**Figure 2.9:** Relative power at the Nørrekær wind farm from observations (blue dots) and predictions (colored lines) with the GM-trained NN.

## BIBLIOGRAPHY

- MHI Vestas Offshore Wind, World's most powerful wind turbine selected for Belgium's largest offshore wind park, 2016. URL: <http://www.mhivestasoffshore.com/norther-foi/>.
- Siemens AG, SWT-8.0-154 Product Brochure, 2016. URL: [https://www.siemens.com/content/dam/internet/siemens-com/global/market-specific-solutions/wind/data\\_sheets/swt-8.0-154-data-sheet-wind-turbine.pdf](https://www.siemens.com/content/dam/internet/siemens-com/global/market-specific-solutions/wind/data_sheets/swt-8.0-154-data-sheet-wind-turbine.pdf).
- Offshore Wind, Ming Yang installs SCD 6.5MW turbine, 2014. URL: <http://www.offshorewind.biz/2014/11/03/ming-yang-installs-scd-6-5mw-turbine/>.
- Adwen, 8 MW platform, 2016. URL: <http://www.adwenoffshore.com/products-services/products/8-mw-turbines/>.
- L. J. Vermeer, J. N. Sørensen, A. Crespo, Wind turbine wake aerodynamics, *Progress in Aerospace Sciences* 39 (2003) 467–510.
- J. F. Ainslie, U. Hassan, H. G. Parkinson, G. J. Taylor, A Wind Tunnel Investigation of the Wake Structure Within Small Wind Turbine Farms, *Wind Engineering* 14 (1990) 24–31.
- L. P. Chamorro, F. Porté-Agel, Effects of Thermal Stability and Incoming Boundary-Layer Flow Characteristics on Wind-Turbine Wakes: A Wind-Tunnel Study, *Boundary-Layer Meteorology* 136 (2010) 515–533.
- T. Y. Chen, L. R. Liou, Blockage corrections in wind tunnel tests of small horizontal-axis wind turbines, *Experimental Thermal and Fluid Science* 35 (2011) 565–569.

- W. Haans, T. Sant, G. van Kuik, G. van Bussel, Measurement of Tip Vortex Paths in the Wake of a HAWT Under Yawed Flow Conditions, *Journal of Solar Energy Engineering* 127 (2005) 456–463.
- P.-Å. Krogstad, P. E. Eriksen, Blind test calculations of the performance and wake development for a model wind turbine, *Renewable Energy* 50 (2013) 325–333.
- T. Cho, C. Kim, Wind tunnel test results for a 2/4.5 scale MEXICO rotor, *Renewable Energy* 42 (2012) 152–156.
- D. Simms, S. J. Schreck, M. Hand, L. J. Fingersh, NREL Unsteady Aerodynamics Experiment in the NASA-Ames Wind Tunnel: A Comparison of Predictions to Measurements, Technical Report NREL/TP-500-29494, 2001.
- H. Snel, J. G. Schepers, B. Montgomerie, The MEXICO project (Model Experiments in Controlled Conditions): The database and first results of data processing and interpretation, *Journal of Physics: Conference Series* 75 (2007) 012014.
- S. McTavish, D. Feszty, F. Nitzsche, Evaluating Reynolds number effects in small-scale wind turbine experiments, *Journal of Wind Engineering and Industrial Aerodynamics* 120 (2013) 81–90.
- B. Sanderse, S. P. van der Pijl, B. Koren, Review of computational fluid dynamics for wind turbine wake aerodynamics, *Wind Energy* 14 (2011) 799–819.
- H. Glauert, *Airplane Propellers*, Springer Berlin Heidelberg, 1935, pp. 169–360.
- R. Gómez-Elvira, A. Crespo, E. Migoya, F. Manuel, J. Hernández, Anisotropy of turbulence in wind turbine wakes, *Journal of Wind Engineering and Industrial Aerodynamics* 93 (2005) 797–814.
- A. Jimenez, A. Crespo, E. Migoya, J. Garcia, Large-eddy simulation of spectral coherence in a wind turbine wake, *Environmental Research Letters* 3 (2008) 15004.

- M. Calaf, C. Meneveau, J. Meyers, Large eddy simulation study of fully developed wind-turbine array boundary layers, *Physics of Fluids* 22 (2010) 1–16.
- J. N. Sørensen, C. W. Kock, A model for unsteady rotor aerodynamics, *Journal of Wind Engineering and Industrial Aerodynamics* 58 (1995) 259–275.
- C. Masson, A. Smaili, C. Leclerc, Aerodynamic analysis of HAWTs operating in unsteady conditions, *Wind Energy* 4 (2001) 1–22.
- C. Alinot, C. Masson, Aerodynamic Simulations of Wind Turbines Operating in Atmospheric Boundary Layer With Various Thermal Stratifications, *ASME 2002 Wind Energy Symposium* (2002) 206–215.
- J. N. Sørensen, W. Z. Shen, Numerical modeling of wind turbine wakes, *Journal of Fluids Engineering* 124 (2002) 393–399.
- N. Troldborg, J. N. Sørensen, R. Mikkelsen, Numerical simulations of wake characteristics of a wind turbine in uniform inflow, *Wind Energy* 13 (2010) 86–99.
- H. Lu, F. Porté-Agel, Large-eddy simulation of a very large wind farm in a stable atmospheric boundary layer, *Physics of Fluids* 23 (2011).
- J. Schluntz, R. H. Willden, An actuator line method with novel blade flow field coupling based on potential flow equivalence, *Wind Energy* 18 (2015) 1469–1485.
- S. Xie, C. Archer, Self-similarity and turbulence characteristics of wind turbine wakes via large-eddy simulation, *Wind Energy* 18 (2015) 18151838.
- M.-C. Hsu, I. Akkerman, Y. Bazilevs, Finite element simulation of wind turbine aerodynamics: validation study using NREL Phase VI experiment, *Wind Energy* 17 (2014) 461–481.
- M. J. Churchfield, S. Lee, J. Michalakes, P. J. Moriarty, A numerical study of the effects of atmospheric and wake turbulence on wind turbine dynamics, *Journal of Turbulence* 13 (2012a) N14.

- M. J. Churchfield, S. Lee, P. J. Moriarty, L. Martinez, S. Leonardi, G. Vijayakumar, J. G. Brasseur, A large-eddy simulation of wind-plant aerodynamics, 50th AIAA Aerospace Sciences Meeting including the New Horizons Forum and Aerospace Exposition, Aerospace Sciences Meetings, 2012b.
- D. H. Wood, Some effects of compressibility on small horizontal-axis wind turbines, *Renewable Energy* 10 (1997) 11–17.
- J. G. Leishman, T. S. Beddoes, A semi-empirical model for dynamic stall, *Journal Of The American Helicopter Society* 34 (1989) 3–17.
- E. Duque, C. van Dam, S. Hughes, Navier-Stokes simulations of the NREL combined experiment phase II rotor, 37th Aerospace Sciences Meeting and Exhibit, Reno (NV), 1999.
- E. Duque, M. D. Burklund, W. Johnson, Navier-Stokes and comprehensive analysis performance predictions of the NREL phase VI experiment, *Journal of Solar Energy Engineering* 125 (2003) 457–467.
- G. Xu, L. Sankar, Effects of transition, turbulence and yaw on the performance of horizontal axis wind turbines, 2000 ASME Wind Energy Symposium, Reno (NV), 2000.
- A. L. Pape, J. Lecanu, 3D Navier-Stokes computations of a stall-regulated wind turbine, *Wind Energy* 7 (2004) 309–324.
- L. Cambier, M. Gazaix, elsA - An efficient object-oriented solution to CFD complexity, 40th AIAA Aerospace Sciences Meeting & Exhibit, Aerospace Sciences Meetings, 2002.
- G. J. Leishman, Principles of helicopter aerodynamics with CD extra, Cambridge University Press, 2006.

- R. E. Wilson, P. B. S. Lissaman, Applied aerodynamics of wind power machines, Oregon State Univ., Corvallis (USA), 1974.
- O. de Vries, Fluid dynamic aspects of wind energy conversion, Technical Report, DTIC Document, 1979.
- W. Z. Shen, R. Mikkelsen, J. N. Sørensen, C. Bak, Tip loss corrections for wind turbine computations, *Wind Energy* 8 (2005) 457–475.
- X. Wang, W. Z. Shen, W. J. Zhu, J. N. Sørensen, J. Chen, Shape optimization of wind turbine blades, *Wind Energy* 12 (2009) 781–803.
- J. F. Manwell, J. G. McGowan, A. L. Rogers, *Wind Energy Explained*, John Wiley & Sons, Ltd, 2010.
- Z. Du, M. Selig, A 3-D stall-delay model for horizontal axis wind turbine performance prediction, 1998 ASME Wind Energy Symposium, Aerospace Sciences Meetings, 1998.
- A. J. Eggers, K. Chaney, R. Digumarthi, An Assessment of approximate modeling of aerodynamic loads on the UAE Rotor, ASME 2003 Wind Energy Symposium, Aerospace Sciences Meetings, 2003.
- L. A. Viterna, D. C. Janetzke, Theoretical and experimental power from large horizontal-axis wind turbines, Technical Report NASA TM-82944, U.S. Department of Energy, 1982.
- J. Jonkman, S. Butterfield, W. Musial, G. Scott, Definition of a 5-MW reference wind turbine for offshore system development, Technical Report NREL/TP-500-38060, National Renewable Energy Laboratory, 2009.
- H. S. Tsien, Two-dimensional subsonic flow of compressible fluids, *Journal of the Aeronautical Sciences* 6 (1939) 399–407.

- T. von Karman, Compressibility effects in aerodynamics, *Journal of the Aeronautical Sciences* 8 (1941) 337–356.
- E. V. Laitone, New compressibility correction for two-dimensional subsonic flow, *Journal of the Aeronautical Sciences* 18 (1951) 350–350.
- H. J. T. Kooijman, C. Lindenburg, D. Winkelaar, E. L. van der Hooft, DOWEC 6 MW Pre-Design: Aero-elastic modeling of the DOWEC 6 MW pre-design in PHATAS, Technical Report DOWEC 10046.009, Energy Research Center of the Netherlands, 2003.
- C. Lindenburg, Aeroelastic modeling of the LMH64-5 blade, Technical Report DOWEC 10083\_001, Energy Research Center of the Netherlands, 2002.
- C. L. Archer, S. Mirzaeisefat, S. Lee, Quantifying the sensitivity of wind farm performance to array layout options using large-eddy simulation, *Geophysical Research Letters* 40 (2013) 4963–4970.
- N. S. Ghaisas, C. L. Archer, S. Xie, S. Wu, E. Maguire, Evaluation of layout and atmospheric stability effects in wind farms using large-eddy simulation, *Wind Energy* 20 (2017) 1227–1240.
- K. Bhaganagar, M. Debnath, The effects of mean atmospheric forcings of the stable atmospheric boundary layer on wind turbine wake, *Journal of Renewable and Sustainable Energy* 7 (2015) 013124.
- B. E. Launder, D. B. Spalding, The numerical computation of turbulent flows, *Computer Methods in Applied Mechanics and Engineering* 3 (1974) 269–289.
- E. E. Khalil, D. B. Spalding, J. H. Whitelaw, The calculation of local flow properties in two-dimensional furnaces, *International Journal of Heat and Mass Transfer* 18 (1975) 775–791.

- B. E. Launder, A. Morse, W. Rodi, D. B. Spalding, Prediction of free shear flows: A comparison of the performance of six turbulence models, Technical Report NASA SP-311, NASA, 1973.
- R. I. Issa, Solution of the implicitly discretised fluid flow equations by operator-splitting, *Journal of Computational Physics* 62 (1986) 40–65.
- U. Schumann, Subgrid scale model for finite difference simulations of turbulent flows in plane channels and annuli, *Journal of Computational Physics* 18 (1975) 376–404.
- N. S. Ghaisas, C. L. Archer, Geometry-based models for studying the effects of wind farm layout, *Journal of Atmospheric and Oceanic Technology* 33 (2016) 481–501.
- C. L. Archer, B. A. Colle, D. L. Veron, F. Veron, M. J. Sienkiewicz, On the predominance of unstable atmospheric conditions in the marine boundary layer offshore of the u.s. northeastern coast, *Journal of Geophysical Research: Atmospheres* 121 (2016) 8869–8885.
- M. O. L. Hansen, J. N. Sørensen, S. Voutsinas, N. Sørensen, H. A. Madsen, State of the art in wind turbine aerodynamics and aeroelasticity, *Progress in Aerospace Sciences* 42 (2006) 285–330.
- J. N. Sørensen, Aerodynamic aspects of wind energy conversion, *Annual Review of Fluid Mechanics* 43 (2011) 427–448.
- Siemens AG, SWT-2.3-93 Product Brochure, 2009. URL: [https://www.energy.siemens.com/mx/pool/hq/power-generation/wind-power/E50001-W310-A102-V6-4A00\\_WS\\_SWT-2.3-93\\_US.pdf](https://www.energy.siemens.com/mx/pool/hq/power-generation/wind-power/E50001-W310-A102-V6-4A00_WS_SWT-2.3-93_US.pdf).
- A. Vassel-Be-Hagh, C. L. Archer, Wind farm hub height optimization, *Applied Energy* 195 (2017) 905–921.
- GWEC, Market Forecast for 2017-2021, 2016. <http://gwec.net/global-figures/market-forecast-2012-2016/>, accessed 2018-03-01.

- M. Z. Jacobson, C. L. Archer, Saturation wind power potential and its implications for wind energy, *Proceedings of the National Academy of Sciences* 109 (2012) 15679–15684.
- K. Marvel, B. Kravitz, K. Caldeira, Geophysical limits to global wind power, *Nature Climate Change* 2 (2012) 1–4.
- A. C. Fitch, J. B. Olson, J. K. Lundquist, Parameterization of wind farms in climate models, *Journal of Climate* 26 (2013) 6439–6458.
- M. Jacobson, C. Archer, W. Kempton, Taming hurricanes with arrays of offshore wind turbines, *Nature Climate Change* 4 (2014).
- Y.-T. Wu, F. Porté-Agel, Large-eddy simulation of wind-turbine wakes: Evaluation of turbine parametrisations, *Boundary-Layer Meteorology* 138 (2011) 345–366.
- S. Xie, C. L. Archer, Self-similarity and turbulence characteristics of wind turbine wakes via large-eddy simulation, *Wind Energy* 18 (2015) 1815–1838.
- C. Yan, C. L. Archer, Assessing compressibility effects on the performance of large horizontal-axis wind turbines, *Applied Energy* 212 (2018) 33–45.
- N. O. Jensen, A note on wind generator interaction, Tech. Note Risø-M-2411, Risø National Laboratory, Denmark, 1983.
- G. C. Larsen, A simple wake calculation procedure, Tech. Note Risø-M-2760, Risø National Laboratory, Denmark, 1988.
- J. F. Ainslie, Calculating the flowfield in the wake of wind turbines, *Journal of Wind Engineering and Industrial Aerodynamics* 27 (1988) 213–224.
- S. Frandsen, R. Barthelmie, S. Pryor, O. Rathmann, S. Larsen, J. Højstrup, M. Thøgersen, Analytical modelling of wind speed deficit in large offshore wind farms, *Wind Energy* 9 (2006) 39–53.

- M. Lei, L. Shiyan, J. Chuanwen, L. Hongling, Z. Yan, A review on the forecasting of wind speed and generated power, *Renewable and Sustainable Energy Reviews* 13 (2009) 915–920.
- K. Hornik, M. Stinchcombe, H. White, Multilayer feedforward networks are universal approximators, *Neural Networks* 2 (1989) 359–366.
- J. Schmidhuber, Deep learning in neural networks: An overview, *Neural Networks* 61 (2015) 85–117.
- M. Carolin Mabel, E. Fernandez, Analysis of wind power generation and prediction using ANN: A case study, *Renewable Energy* 33 (2008) 986–992.
- R. Blonbou, Very short-term wind power forecasting with neural networks and adaptive Bayesian learning, *Renewable Energy* 36 (2011) 1118–1124.
- S. Kelouwani, K. Agbossou, Nonlinear model identification of wind turbine with a neural network, *IEEE Transactions on Energy Conversion* 19 (2004) 607–612.
- T. G. Barbounis, J. B. Theocharis, M. C. Alexiadis, P. S. Dokopoulos, Long-term wind speed and power forecasting using local recurrent neural network models, *IEEE Transactions on Energy Conversion* 21 (2006) 273–284.
- S. Li, Wind power prediction using recurrent multilayer perceptron neural networks, in: 2003 IEEE Power Engineering Society General Meeting (IEEE Cat. No.03CH37491), volume 4, 2003, p. 2330 Vol. 4.
- N. S. Ghaisas, C. L. Archer, S. Xie, S. Wu, E. Maguire, Evaluation of layout and atmospheric stability effects in wind farms using large-eddy simulation, *Wind Energy* 20 (2017) 1227–1240.
- A. Miller, E. Muljadi, D. S. Zinger, A variable speed wind turbine power control, *IEEE Transactions on Energy Conversion* 12 (1997) 181–186.

- Y.-T. Wu, F. Porté-Agel, Simulation of turbulent flow inside and above wind farms: Model validation and layout effects, *Boundary-Layer Meteorology* 146 (2013) 181–205.
- N. S. Ghaisas, C. L. Archer, Geometry-based models for studying the effects of wind farm layout, *Journal of Atmospheric and Oceanic Technology* 23 (2016) 481–501.
- R. S. Sutton, Two problems with backpropagation and other steepest-descent learning procedures for networks, in: *Proceedings of the Eighth Annual Conference of the Cognitive Science Society*, Erlbaum, 1986, pp. 823–831.
- B. T. Polyak, Some methods of speeding up the convergence of iteration methods, *USSR Computational Mathematics and Mathematical Physics* 4 (1964) 1–17.
- J. Duchi, E. Hazan, Y. Singer, Adaptive subgradient methods for online learning and stochastic optimization, *Journal of Machine Learning Research* 12 (2011) 2121–2159.
- M. D. Zeiler, ADADELTA: An adaptive learning rate method, *CoRR* abs/1212.5701 (2012).
- T. Tieleman, G. Hinton, RMSprop, 2012. Available at [http://www.cs.toronto.edu/~tijmen/csc321/slides/lecture\\_slides\\_lec6.pdf](http://www.cs.toronto.edu/~tijmen/csc321/slides/lecture_slides_lec6.pdf).
- D. P. Kingma, J. Ba, Adam: A method for stochastic optimization, *CoRR* abs/1412.6980 (2014).
- C. M. Bishop, *Pattern recognition and machine learning*, 2006.
- A. Creech, W.-G. Frü, A. E. Maguire, Simulations of an offshore wind farm using large-eddy simulation and a torque-controlled actuator disc model, *Surveys in Geophysics* 36 (2015) 427–481.
- A. M. Foley, P. G. Leahy, A. Marvuglia, E. J. McKeogh, Current methods and advances in forecasting of wind power generation, *Renewable Energy* 37 (2012) 1–8.

## Appendix A

### SIMULATIONS OF ATMOSPHERIC BOUNDARY FLOW

A test to validate the compressible framework is a simple atmospheric boundary layer (ABL) flow with realistic wind speeds. Because the Mach number approaches zero, the simulation results using the compressible and the conventional incompressible frameworks should converge.

The two simulations were carried out in a Cartesian computational domain with streamwise, spanwise, and vertical lengths of 1890, 882, and 441 m, respectively. Using the diameter of the NREL 5-MW wind turbine as reference ( $D=126$  m), the domain size can be expressed in non-dimensional form as  $15D \times 7D \times 3.5D$  (Fig. A.1). The computational domain is divided in each direction into  $N_x \times N_y \times N_z = 240 \times 192 \times 96$  grid points of sizes  $\Delta x \times \Delta y \times \Delta z = 7.9 \text{ m} \times 4.6 \text{ m} \times 4.6 \text{ m}$ . No wind turbine is used in this simulation.

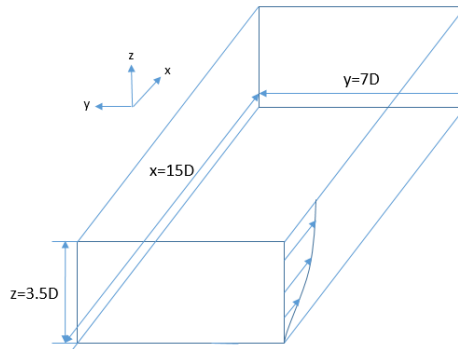


**Figure A.1:** Computational domain for atmospheric boundary layer flow. Domain sizes are expressed as multiples of the diameter of the reference NREL 5-MW wind turbine ( $D=126$  m).

A constant geostrophic wind speed of  $15 \text{ m s}^{-1}$  is imposed at the domain top and periodic boundary conditions are used at the spanwise and streamwise boundaries, so

that the two frameworks simulate an infinitely-large atmospheric boundary layer. The Reynolds number is sufficiently high to neglect molecular viscosity, except at the first grid point off the ground, where the Schumann’s wall model is imposed (Schumann, 1975). The turbulent closure is the k-epsilon model, the simulations are carried out for 11,000 seconds, which is long enough for turbulence to become fully developed to capture the log-law of the ABL.

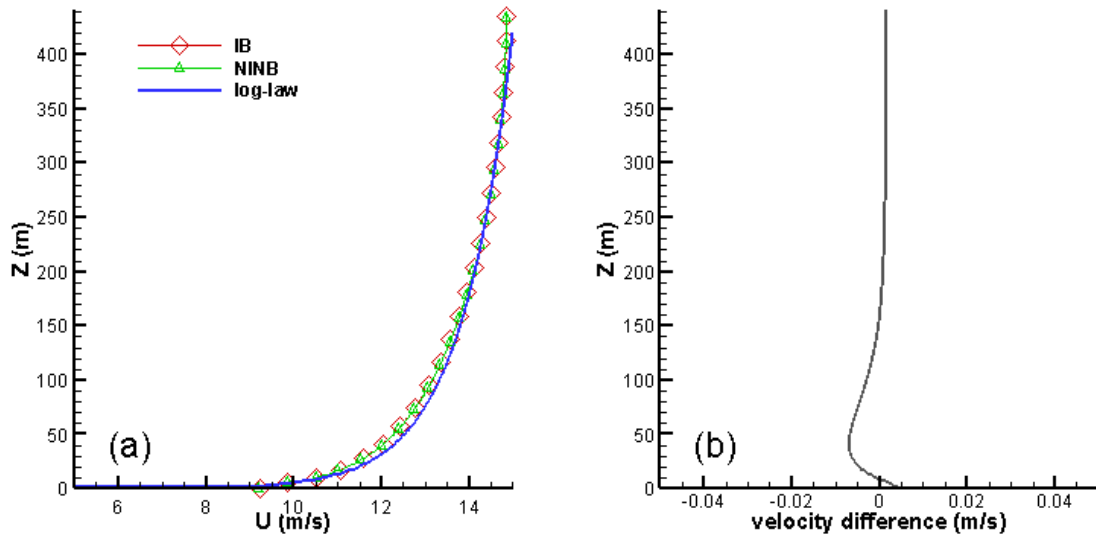


**Figure A.2:** (a) Horizontally-averaged wind speed of the incompressible and compressible frameworks, compared with the theoretical log-law. (b) Horizontally-averaged wind speed difference between the two frameworks (incompressible minus compressible).

Both the conventional incompressible and the compressible framework capture the log-law of the ABL very well. No significant differences can be found between the vertical profiles of horizontally-averaged wind speeds from the incompressible, compressible, and theoretical log-law (Fig. A.2). The magnitude of the difference is, at most, of the order of  $10^{-4}$  of the geostrophic wind speed near the surface. It can be concluded that the compressible framework has the ability to capture low Mach number flows correctly and consistently with the conventional incompressible framework.

Appendix B  
COPYRIGHT PERMISSION

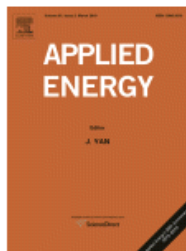


RightsLink®

Home

Create Account

Help



**Title:** Assessing compressibility effects on the performance of large horizontal-axis wind turbines  
**Author:** Chi Yan, Cristina L. Archer  
**Publication:** Applied Energy  
**Publisher:** Elsevier  
**Date:** 15 February 2018  
© 2017 Elsevier Ltd. All rights reserved.

**LOGIN**  
If you're a [copyright.com](#) user, you can login to RightsLink using your [copyright.com](#) credentials. Already a [RightsLink](#) user or want to [learn more?](#)

Please note that, as the author of this Elsevier article, you retain the right to include it in a thesis or dissertation, provided it is not published commercially. Permission is not required, but please ensure that you reference the journal as the original source. For more information on this and on your other retained rights, please visit: <https://www.elsevier.com/about/our-business/policies/copyright#Author-rights>

BACK

CLOSE WINDOW

Copyright © 2018 [Copyright Clearance Center, Inc.](#) All Rights Reserved. [Privacy statement](#). [Terms and Conditions](#). Comments? We would like to hear from you. E-mail us at [customer@copyright.com](mailto:customer@copyright.com)